Genetically Encoded and Modular SubCellular Organelle Probes (GEM-SCOPe) reveal lysosomal and mitochondrial dysfunction driven by *PRKN* knockout

Camille Goldman[1-6], Tatyana Kareva[1-6], Lily Sarrafha[1-6], Braxton R. Schuldt[1-5], Abhishek Sahasrabudhe[1-3], Tim Ahfeldt[1-6 **], Joel W. Blanchard[1-7 *]

1. Icahn School of Medicine, Mount Sinai, New York, NY, USA
2. Nash Family Department of Neuroscience, Mount Sinai, New York, NY, USA
3. Friedman Brain Institute, Mount Sinai, New York, NY, USA
4. Ronald M. Loeb Center for Alzheimer's Disease, Mount Sinai, New York, NY USA
5. Black Family Stem Cell Institute, Mount Sinai, New York, NY, USA
6. Aligning Science Across Parkinson's (ASAP) Collaborative Research Network, Chevy Chase, MD, USA
7. Lead Contact

* Corresponding author

** 2nd corresponding author

Correspondence: joel.blanchard@mssm.edu

Correspondence: ahfeldt@gmail.com

Summary

Cellular processes including lysosomal and mitochondrial dysfunction are implicated in the development of many diseases. Quantitative visualization of mitochondria and lysosomes is crucial to understand how these organelles are dysregulated during disease. To address a gap in live-imaging tools, we developed GEM-SCOPe (Genetically Encoded and Modular SubCellular Organelle Probes), a modular toolbox of fluorescent markers designed to inform on localization, distribution, turnover, and oxidative stress of specific organelles. We expressed GEM-SCOPe in differentiated astrocytes and neurons from a human pluripotent stem cell *PRKN*-knockout model of Parkinson's disease and identified disease-associated changes in proliferation, lysosomal distribution, mitochondrial transport and turnover, and reactive oxygen species. We demonstrate GEM-SCOPe is a powerful panel that provide critical insight into the subcellular mechanisms underlying Parkinson's disease in human cells. GEM-SCOPe can be expanded upon and applied to a diversity of cellular models to glean an understanding of the mechanisms that promote disease onset and progression.

Introduction

Parkinson's Disease (PD) is a common neurodegenerative disease that robs individuals of their motor and cognitive functions, affecting over 10 million people worldwide and with an estimated 90,000 new diagnoses in the United States each year[1]. PD is clinically characterized by bradykinesia, resting tremor, rigidity, and postural instability[2-5] and pathologically characterized by the loss of dopaminergic neurons in the substantia nigra pars compacta and buildup of intracellular deposits of α-synuclein into insoluble protein aggregates called Lewy Bodies[2,6-8]. From the first pathological descriptions of PD in the mid-20th century, advancements in many fields, including histology, genetics, cell biology, and neurology enabled insight into many aspects of the disease, from determining genetic and environmental risk factors and mapping disease progression to identifying pathways and proteins to target therapeutically. Despite great progress, there is still incomplete understanding of the cellular dysfunction that precedes and contributes to chronic neuronal death.

This limited advancement arises in part due to the absence of tools used to track molecular and cellular changes in real-time throughout disease progression. Studies on human post-mortem brain tissue are largely representative of end-stage disease states, making it difficult to dissect which phenotypes are a primary, causative effect and which phenotypes are a secondary response[9]. Mouse models offer more opportunities to study multiple time points throughout disease progression as motor and cognitive symptoms can be monitored over time. However, targeting specific cell types in mice remains technically challenging and time-consuming. Emerging technologies such as the miniscope allow continuous monitoring of fluorescence-based readouts on a cellular level in live mouse and rat brains[10-12]. However, the type of readout from the miniscope has been restricted to neuronal activity from fluorescent calcium sensors and resolution along the z-axis remains a limiting factor in analyzing deeper cortical tissue.

56 Regardless of such technologies, current genetic rodent models of PD fail to completely
57 recapitulate human disease and lack key pathological hallmarks. Drug-induced models can
58 recapitulate late-stage disease phenotypes and behaviors, but due to their acute onset, are
59 inadequate to study the gradual accumulation of cellular dysfunction that precedes clinical
60 presentation[13,14]. Advancements in induced pluripotent stem cell (iPSC) differentiation and
61 CRISPR/Cas9 genome editing have led to the emergence of genetic cellular models of PD[15-18].
62 These models enable researchers to study the effects of genetic and environmental factors on
63 specific human cell populations relevant to PD.

64 Cellular models of PD provide an exciting opportunity to study subcellular changes and responses
65 to stress or treatment in live cells. Cells can be genetically engineered to express fluorescent
66 proteins that can then be visualized by microscopy in live cells. The applicability of GFP as a
67 reporter gene was immediately appreciated after its identification and isolation in 1962[19]. Since
68 then, hundreds of fluorophores have been developed by introducing mutations to naturally
69 occurring fluorophores isolated from sea anemones and jellyfish to modulate fluorescence
70 intensity, half-life, and excitation/emission spectra[20]. Additional fluorophores have been
71 developed as biosensors, by fluorescing or changing fluorescence emission in the presence of a
72 certain ligand or under specific cellular conditions[20-25]. Cells can express these fluorophores with
73 virtually limitless possibilities with regards to subcellular localization, cell-type specific expression,
74 and temporally controlled expression. Genetically encoded fluorescent proteins can be used to
75 follow a population of cells as they change due to aging, genetics, or environmental stressors and
76 stimuli.

77 PD has a complex genetic architecture underlying the disease. Over 90% of PD cases are
78 idiopathic; over 90 genetic risk loci have been identified by GWAS, but any of those individual
79 variants confer little risk on their own[26]. The remaining 10% of PD cases can be linked to highly
80 penetrant mutations in a handful of genes. While extremely rare, studying the function of these

genes and their impact on cellular processes sheds light on the fundamental pathways that drive PD pathogenesis. Here, we focus on the *PRKN* gene. Autosomal recessive loss of function mutations in *PRKN* are the most frequent known genetic cause of early onset cases of PD, accounting for about 15% of PD cases with onset before the age of 50[27-30]. *PRKN* encodes for the protein PRKN, an E3 ubiquitin ligase associated with mitochondria. PRKN directs the ubiquitination of outer mitochondrial membrane proteins on damaged mitochondria, targeting them for degradation via the autophagy-lysosomal pathway (mitophagy)[31-33]. While the function of PRKN is well understood, it is still unclear how loss of PRKN function leads to the gradual disease progression of early onset PD. It is believed that neurodegeneration can begin over 20 years before clinical onset, with a prolonged prodromal phase associated with several non-motor symptoms. Thus, it is crucial to study models of early disease to understand what cellular disturbances in the prodromal phase culminate in neurodegeneration.

Here, we present GEM-SCOPe (**G**enetically **E**ncoded and **M**odular **S**ub**C**ellular **O**rganelle **P**robes), an expandable panel of genetically encoded reporters to track and quantify the subcellular phenotypes in live cells. We developed a library of constructs that localize specifically to the nucleus, mitochondria, and lysosomes and included fluorophores with a variety of emission spectra or biosensor capabilities. All the lentiviral constructs were developed in the same backbone vector to be modular, enabling any component, be it promotor, localization signal, fluorophore, or antibiotic resistance, to be easily removed or replaced. We validated the fluorophores with live-imaging of human induced pluripotent stem cell (hiPSC)-derived midbrain astrocytes employing existing chemical dyes and chemical perturbations. We then applied GEM-SCOPe to hiPSC-derived astrocytes and neurons from a *PRKN*-knockout model of PD,[15] to demonstrate the applicability in detecting genetically-mediated effects in disease models. This revealed previously unseen changes in cellular proliferation, lysosomal distribution, mitochondrial motility and turnover, and reactive oxygen species production. Our results demonstrate the

106 widespread utility of GEM-SCOPe to study a variety of translationally important subcellular
107 changes. The modular, combinatorial flexibility of GEM-SCOPe can be adapted to investigate any
108 disease, and, therefore, it is a critical new resource that can be broadly applied in
109 neurodegenerative research and beyond.

110

111 Results

112 Building a modular toolbox for the subcellular localization of 113 genetically encoded fluorophores

114 We developed GEM-SCOPe for live-cell imaging of subcellular organelle dynamics. We aimed to
115 produce a system that is highly modular to easily customize the expression, localization,
116 fluorescence, and selection for any given experimental need. We started with the FUW
117 backbone[34], a 3rd generation lentivirus backbone with a ubiquitin C promoter for high, ubiquitous
118 expression of the transgene across cell types[34,35] and a woodchuck hepatitis virus post-
119 transcriptional regulatory element (WPRE) for improved lentiviral expression[34,36,37]. The designed
120 lentiviral constructs contain four components: promoter, localization sequence, fluorophore, and
121 antibiotic resistance (**Fig. 1A**). The content of these four components can be mixed and matched
122 to generate a library of lentiviral constructs to fit a diverse field of experimental needs. To generate
123 constructs *de novo*, components were combined and inserted into the plasmid via Gibson
124 assembly (**Fig. 1B, top**). Restriction sites were kept between each domain, so each component
125 or group of components could be excised via restriction digest and replaced with a different
126 component, either by restriction site cloning or Gibson assembly (**Fig. 1B, bottom**). Thus, each
127 component of the lentiviral plasmid can be removed or replaced to accommodate features such

128 as cell-type specificity with cell-type specific promoters, alternative subcellular localization, and
129 unique fluorophores.

130 The FUW backbone has a ubiquitin C promoter, but this can be replaced with lineage or cell-type-
131 specific promoters for selective expression in specific cell types or with drug-inducible promoters
132 to temporally control when the construct is transcribed (**Fig. S1A**). Subcellular localization is
133 determined by including the whole or partial coding sequence of a peptide with a known and
134 specific subcellular localization. This domain can be omitted to produce a fluorophore expressed
135 in the cytoplasm. The fluorophore component of the construct offers the most flexibility, from basic
136 fluorescent proteins to more complex fluorophores that change fluorescent excitation and/or
137 emission wavelength with time or environment. All plasmids generated for GEM-SCOPe have
138 been deposited to Addgene (**Table S1**).

139 We developed GEM-SCOPe constructs to localize fluorophores to the cytoplasm (no tag), nucleus
140 (H2B-tag), mitochondria (COX8A-tag), and lysosome (LAMP1-tag) (**Fig. 1C**). Fluorophore
141 localization was validated using commercially available live cellular dyes. Nuclear localization was
142 achieved by fusing fluorophores to the C-terminus of histone 2B (H2B). H2B is an integral
143 chromatin protein that is found in all cells and is localized specifically to the nucleus[38,39]. H2B
144 fused to mTagBFP2, a blue fluorophore, (H2B-mTagBFP2) co-localizes with DRAQ5, a far-red
145 live-cell nuclear dye[40] (**Fig. 1C, top**; Mander's coefficient > 0.99±0.0001). In addition to the
146 mTagBFP2 construct, we also developed lentiviral plasmids with H2B fused to Emerald (green;
147 H2B-Emerald) and mCherry (red; H2B-mCherry) (**Fig. 1A, S1B**).

148 To localize fluorophores to the lysosome, we utilized the N-terminal peptide sequence of
149 lysosomal-associated membrane protein 1 (LAMP1), a major component of lysosomal
150 membranes that plays a key role in lysosomal biogenesis and homeostasis. The N-terminus of
151 LAMP1 fused to mCherry (LAMP1-mCherry) co-localizes with LysoTracker (Thermo Scientific)
152 (**Fig. 1C, middle**; Mander's coefficient = 0.92±0.03). LysoTracker is a fluorophore that is partially

153 protonated at neutral pH and can readily cross membranes; once protonated it can no longer
154 diffuse so the fluorescent signal gets trapped in acidic compartments, including, but not limited to,
155 the lysosome[41,42]. Overexpression of LAMP1 is associated with numerous cancers and cancer
156 metastasis[43-46]. By only using a partial sequence of LAMP1 and not the full peptide sequence, we
157 are able to target the fluorophore specifically to the lysosome without increasing the expression
158 of endogenous LAMP1 (**Fig. S1C**). We also developed lentiviral plasmids with the LAMP1
159 targeting sequence fused to Emerald (green; LAMP1-Emerald; **Fig. 1A, 1D**).

160 Finally, mitochondrial localization was achieved using the mitochondrial targeting sequence of
161 COX8A. COX8A is a nuclear-encoded subunit of cytochrome-c oxidase (Complex IV) in the
162 electron transport chain[47,48]. The first 25 amino acid residues of the COX8A peptide sequence
163 target the peptide to the mitochondrial inner membrane and are widely used to specifically localize
164 proteins and fluorophores to the mitochondria[49-51]. To confirm mitochondrial specificity of COX8A-
165 Emerald we compared localization with MitoTracker (Thermo Scientific), a dye that accumulates
166 in the mitochondria due to the negative membrane potential of the inner mitochondrial
167 membrane[41,52]. The mitochondrial targeting sequence fused to an Emerald fluorophore (COX8A-
168 Emerald) exhibited significant co-localization with MitoTracker (**Fig. 1C, bottom**; Mander's
169 coefficient = 0.97±0.003). We developed lentiviral plasmids with the COX8A targeting sequence
170 fused to mCherry (red; COX8A-mCherry; **Fig. 1A, 1D**), Timer (green/red; COX8A-Timer; **Fig. 1A,**
171 **Fig. 5**), and Lemon (cyan/yellow; COX8A-Lemon; **Fig. 1A, Fig. S1D, E**).

172 Once the localization strategies were finalized, we swapped out the fluorophores with different
173 fluorescent proteins that are excited and emitted at alternative wavelengths. Mixing localization
174 sequences and fluorophores with unique emission spectra allows simultaneous imaging of
175 multiple sub-cellular processes in the same cells such as mitochondrial network and lysosomal
176 distribution (**Fig. 1D**). Utilizing a combination of subcellular localization and diverse fluorophores,
177 we developed GEM-SCOPe, a fluorescent, live-cell imaging toolbox of lentiviral constructs that

178 were systematically validated to quantify cellular proliferation, lysosomal distribution, and
179 mitochondrial dynamics in human Parkinson's disease astrocytes.

180

181 H2B-fused fluorophores offer improvements for efficiently
182 labelling nuclei for multi-day live-cell assays

183 Quantification of cellular phenotypes by fluorescence microscopy is dependent on normalization
184 to total cell number. This is often accomplished by counting the number of nuclei. A few fluorescent
185 dyes that can cross the cellular and nuclear membranes of live cells and bind specifically to DNA
186 are commercially available. While efficient for short-term and end-point assays, such dyes
187 intercalate in DNA and therefore have cytotoxic and mutagenic effects[53,54]. Furthermore, nuclear
188 dyes do not remain contained within the nuclear compartment, and their signal leaches into the
189 cytoplasm in just a few hours after exposing the cells. The cytotoxicity and loss of precise labeling
190 over time render these dyes less useful for long-term microscopy or cell-tracking experiments. To
191 address these concerns, we developed lentiviral constructs expressing nuclear-localized
192 fluorophores by fusing the nucleus-specific histone protein, H2B, with either mTagBFP2, Emerald,
193 or mCherry (**Fig. 1C, 2A**). Human induced pluripotent stem-cell (hiPSC)-derived astrocytes
194 transfected with H2B-mTagBFP2 were co-stained with DRAQ5, a far-red DNA-stain for live cells.
195 The localization of the two nuclear signals was compared 1 hours and 24 hours after the addition
196 of DRAQ5. Immediately after adding DRAQ5, there was no difference between the DRAQ5 stain
197 and the H2B-mTagBFP2 (2-way ANOVA with Tukey's HSD; adj-p = 0.35) (**Fig. 2B, C**). Over the
198 experimental period, the DRAQ5 signal spread significantly (19±2% extranuclear; adj-p < 0.0001),
199 while the extranuclear H2B-mTagBFP2 signal did not significantly change (adj-p = 0.95) (**Fig. 2B,
200 C**). Although the human eye can still readily distinguish the nucleus from the extranuclear stain in
201 the DRAQ5 images, image analysis programs that rely on grey values for segmentation often fail

202 to correctly differentiate the true nuclear signal from the extranuclear signal. Thus, lentiviral
203 constructs expressing nuclear-localized fluorophores, such as the demonstrated H2B-
204 mTagBFP2, can provide better alternatives for long-term live-imaging experiments with multiple
205 time points.

206

207 H2B-fused fluorophores reveal increased cellular proliferation 208 in PRKN knockout astrocytes

209 While dopaminergic neuron death is the predominant cellular outcome in Parkinson's Disease
210 (PD), other cell types in the brain may change cell cycle regulation under neurotoxic conditions.
211 Tracking cell numbers to monitor proliferation, senescence, or death in vitro can help researchers
212 understand how different cell populations are responding to neurotoxic stress or potential
213 therapeutic strategies.

214 First, we validated that our nuclear-localized construct, H2B-Emerald, could be used to track
215 cellular proliferation. The proliferation of H2B-Emerald transduced hiPSC-derived astrocytes was
216 induced using fetal bovine serum (FBS) or blocked by inhibiting the proteasome with MG-132.
217 Astrocyte proliferation was measured by changes in the number of H2B-Emerald nuclei. As
218 expected, the astrocytes treated with FBS proliferated twice as rapidly as the untreated astrocytes
219 over 48 hours (2-way ANOVA with Tukey's HSD, p-adj = 0.005, **Fig. S2**), while the astrocytes
220 treated with MG-132 did not significantly proliferate over the same period (adj-p = 0.08, **Fig. S2**).
221 Thus, the GEM-SCOPe H2B-fluorophore fusion proteins can be used to track cellular proliferation
222 over multiple days in live cell cultures.

223 To examine the effect of loss of *PRKN* on astrocyte proliferation, we transduced wild-type
224 (*PRKN*$^{+/+}$) astrocytes with H2B-Emerald and isogenic *PRKN* knockout (*PRKN*$^{-/-}$) astrocytes (**Fig.**

225 **S3A**) with H2B-mCherry (**Fig. 2D**). Leveraging the modularity of GEM-SCOPe, we were able to
226 mix the two astrocyte populations together and track their proliferation simultaneously. Over 48
227 hours, the *PRKN*$^{-/-}$ population increased significantly (2-way ANOVA with Tukey's HSD, p-adj =
228 0.03; **Fig. 2E, F**) while the *PRKN*$^{+/+}$ population did not proliferate in the same period (2-way
229 ANOVA with Tukey's HSD, p-adj = 0.4; **Fig. 2E, F**). Surprisingly, these results contradict mouse
230 studies that found that PRKN-null mice had decreased astroglia proliferation[55]. However, PRKN
231 has been widely described as a tumor suppressor, with loss-of-function mutations arising in a
232 variety of cancers, including glioblastomas[56-58]. Studies on PRKN in the context of cancer have
233 demonstrated that PRKN regulates the degradation of cyclins and cyclin-dependent kinases
234 involved in the G1/S transition, the loss of which promotes unchecked proliferation[57,59,60]. It has
235 previously been hypothesized that the outcome of loss-of-function PRKN mutations are highly
236 cell-context dependent; the increased half-life of cyclins leads to cancer in mitotically competent
237 cells while the same cyclins may promote apoptosis upon cell cycle reentry in post-mitotic cells,
238 such as neurons[57,61-64]. Our results in human astrocytes highlight the importance of studying
239 disease-relevant human cell types to capture the intricacies and nuances specific to the human
240 brain that could contribute to PD.

241

242 LAMP1-localized fluorophores reveal changes in lysosomal 243 distribution in response to chemical and genetic stressors

244 Lysosomal dysfunction is widely implicated in PD and other forms of neurodegeneration. Several
245 PD-risk and familial genes are involved in the autophagy-lysosomal-endosomal pathway[65-67], and
246 many hallmarks of lysosomal dysfunction associated with familial PD are present in idiopathic PD
247 [66,68,69]. Disruption to the autophagy-lysosomal-endosomal pathway is of broad importance in PD
248 and there is a crucial need to study lysosomal function and dysfunction in the context of PD

249 pathogenesis. As described above, we fused the N-terminus of LAMP1 to a fluorophore (Emerald
250 or mCherry) to specifically target the fluorescent signal to the lysosome (**Fig. 1C, 3A**). To validate
251 the GEM-SCOPe LAMP1-mCherry signal responds to lysosomal stress, hiPSC-derived
252 astrocytes transduced with LAMP1-mCherry lentivirus were exposed to bafilomycinA1 (BafA1) for
253 15 hours. BafA1 inhibits lysosomal proton pump V-ATPases, which blocks autophagosome-
254 lysosome fusion and lysosomal acidification, impairing lysosomal function [70,71]. hiPSC-derived
255 astrocytes were simultaneously transduced with a non-localized Emerald fluorophore lentivirus,
256 to provide a cell body marker. We used CellProfiler [72] to evaluate the lysosomal number, size, and
257 distribution within each cell. Compared to vehicle (DMSO) treatment, treatment with BafA1
258 increased the number of LAMP1-mCherry vesicles (unpaired t-test, $p = 0.029$; **Fig. 3B, C**), but
259 did not affect lysosome size (unpaired t-test, $p = 0.16$, **Fig. 3B, C**). Treatment with BafA1 altered
260 the distribution of lysosomes within the astrocytes. Astrocytes treated with BafA1 had a more
261 dispersed distribution of LAMP1-mCherry signal, with only 40.0±2.0% concentrated in the
262 perinuclear area, in contrast to 62.4±7.5% in vehicle-treated astrocytes (unpaired t-test, $p =$
263 0.0012; **Fig. 3B, C**). Perinuclear and juxtanuclear lysosomes have been posited to be more acidic
264 than peripheral lysosomes[73]. Lysosomal distribution can also be affected by cytosolic pH, with
265 acidification promoting the spreading of lysosomes away from the nucleus[74-76]. Since BafA1
266 inhibits V-ATPases responsible for establishing and maintaining lysosomal pH, the redistribution
267 of lysosomes away from the nucleus upon BafA1 treatment might reflect a change in lysosomal
268 or cytosolic pH, and therefore lysosomal function, in the treated astrocytes.

269 In addition to its role in ubiquitinating damaged mitochondria for degradation via the autophagy-
270 lysosomal pathway[31-33], PRKN has been shown to regulate endosome organization[77] and
271 mitochondria-lysosome contact sites. Although it has been reported that *PRKN* knockout in
272 hiPSC-derived dopaminergic neurons leads to an increase in lysosome number and size
273 compared to isogenic, wild-type dopaminergic neurons[78], the effect of *PRKN* knockout on

274 lysosomes on human astrocytes is largely unknown. Due to PRKN's role in regulating the
275 autophagy-lysosomal pathway, we hypothesized *PRKN*$^{-/-}$ in human astrocytes would disrupt
276 lysosomal dynamics. To test this hypothesis, we applied the same CellProfiler analysis on
277 *PRKN*$^{+/+}$ and *PRKN*$^{-/-}$ hiPSC-derived astrocytes transduced with GEM-SCOPe Emerald and
278 LAMP1-mCherry lentivirus. *PRKN*$^{-/-}$ astrocytes had half as many LAMP1-mCherry vesicles per
279 cell compared to *PRKN*$^{+/+}$ astrocytes (unpaired t-test, $p = 0.003$, **Fig. 3D, E**). Additionally, the
280 *PRKN*$^{-/-}$ lysosomes were smaller than the *PRKN*$^{+/+}$ lysosomes (unpaired t-test, $p = 0.052$, **Fig. 3D,**
281 **E**). Finally, the *PRKN*$^{-/-}$ astrocytes had a decrease in perinuclear LAMP1-mCherry, with only
282 38±4% of LAMP1-mCherry signal located in the perinuclear area, compared to 45±3% in
283 *PRKN*$^{+/+}$ (unpaired t-test, $p = 0.005$, **Fig. 3D, E**). Our results utilizing our GEM-SCOPe LAMP1-
284 mCherry fluorophore suggest that lysosomal number and distribution in astrocytes is altered upon
285 loss of *PRKN*. However, further studies to examine lysosomal content and activity are needed to
286 understand the mechanisms by which lysosomes are affected, the implications of this effect on
287 neuron death, and how this could differ from observations in other cell types.

288

289 Mitochondria-localized fluorophores capture mitochondrial 290 fragmentation and alterations in mitochondrial trafficking 291 along PRKN knockout dopaminergic neuron axons

292 Much like lysosomal dysfunction, mitochondrial dysfunction is implicated in PD and
293 neurodegeneration. Therefore, monitoring mitochondrial network dynamics in response to stimuli
294 and stress is important in understanding neurodegenerative diseases. As described above, we
295 fused the N-terminus of the mitochondrial protein COX8A to a fluorophore (Emerald or mCherry)
296 to localize the fluorophore specifically to the mitochondria (**Fig. 1C, 4A**). To validate that GEM-

297 SCOPe COX8A localized fluorophores reflect changes to mitochondrial morphology, we induced
298 mitochondrial stress by treating hiPSC-derived astrocytes transduced with the COX8A-mEmerald
299 lentivirus with 2μM oligomycin for 4 hours. Mitochondrial stress induces fragmentation of the
300 mitochondrial network, which facilitates mitophagy, but also decreases mitochondrial network
301 respiratory capacity[79,80]. Oligomycin, an inhibitor of ATP synthase, is a known inducer of
302 mitochondrial fragmentation. Treatment with oligomycin induced mitochondrial fragmentation
303 when compared to vehicle-treated astrocytes. The average area of mitochondria was reduced
304 from 1.04 μm^2 in vehicle-treated astrocytes to 0.80 μm^2 in oligomycin-treated astrocytes (1-way
305 ANOVA with Dunett's Test, p-adj = 0.0002; **Fig. 4B, C left)**, and average branch length was
306 reduced from 1.28 μm in vehicle-treated astrocytes to 0.90 μm in oligomycin treated astrocytes
307 (1-way ANOVA with Dunett's Test, p-adj < 0.0001; **Fig. 4B, C middle)**, as expected from a more
308 fragmented mitochondrial network. The aspect ratio is the ratio of the mitochondrial length to
309 width. An aspect ratio of 1 indicates a perfect circle, while larger aspect ratios indicate longer and
310 narrower shapes. The mean aspect ratio decreased from 2.52 in vehicle-treated astrocytes to
311 2.14 in oligomycin-treated astrocytes (1-way ANOVA with Dunett's Test, p-adj < 0.0001; **Fig. 4B,**
312 **C right**), another indicator that mitochondria are fragmenting upon oligomycin treatment. Metrics
313 of mitochondrial network fragmentation (mitochondrial area, branch length, and aspect ratio) are
314 all affected in a dose-dependent manner, with increasing concentrations of oligomycin having
315 increasingly more severe effects on mitochondrial network fragmentation (**Fig. S4**).

316 The transport of mitochondria along neuronal axons is critical for proper synaptic function and
317 neurotransmitter release. We hypothesized *PRKN*$^{-/-}$ may impair axonal mitochondrial transport.
318 To investigate this hypothesis, we transduced wild-type (*PRKN*$^{+/+}$) and *PRKN* knock-out (*PRKN*$^{-/-}$
319) hiPSC-derived midbrain organoids with COX8A-mEmerald. To facilitate imaging of axonal
320 mitochondrial transport, we generated radial axonal arbors by splatting organoids onto the surface
321 of a plate and allowing the axons to grow out[81]. On day 164 of organoid differentiation, fluorescent

322 mitochondria were imaged at high magnification over several minutes to monitor the movement
323 of mitochondria along these axons (**Fig. 4D; Video S1**). In the anterograde direction (moving
324 away from the soma), *PRKN*$^{-/-}$ mitochondria moved only 20% of the distance covered by *PRKN*$^{+/+}$
325 mitochondria (Welch's t-test, $p < 0.0001$, **Fig. 4E left**) and took 50% longer (unpaired t-test, $p =$
326 0.005; **Fig. 4E right**). Retrograde-moving mitochondria moved the same distance (unpaired t-
327 test, $p = 0.59$, **Fig. 4F left)** but the *PRKN*$^{-/-}$ mitochondria moved for 150% longer compared to the
328 *PRKN*$^{+/+}$ mitochondria (Welch's t-test, $p = 0.02$; **Fig. 4F right**). PRKN has previously been
329 implicated in mitochondrial transport due to its ubiquitination of mitochondrial motor adaptor
330 complexes[82]. Our results demonstrate that PRKN loss of function impairs mitochondrial trafficking
331 in human neurons, likely reducing the delivery of functional mitochondria synaptic extremities and
332 ultimately compromising neuronal function.

333

334 Dynamic fluorophores measure deficiencies in mitochondrial 335 turnover and glutathione reduction potential in PRKN- 336 knockout astrocytes

337 We demonstrated the utility of single excitation and emission wavelengths to discern phenotypes
338 regarding cellular and subcellular dynamics. Numerous groups have developed fluorophores that
339 change emission wavelengths under certain conditions or circumstances. We introduced several
340 multi-emission fluorophores into GEM-SCOPe to enable quantification of organelle turnover,
341 acidification, and oxidation, in addition to the localization information described with the previous
342 fluorophores.

343 Fluorescent Timer is a mutated dsRed protein that irreversibly shifts its fluorescence emission
344 from green to red due to tyrosine oxidation and can be used as a molecular clock to track protein

345 turnover (**Fig. 5A**).[22] We, therefore, localized GEM-SCOPe-Timer to the mitochondria (COX8A-
346 Timer), to further investigate mitochondrial turnover[83,84] (**Fig. 5B**). To first validate COX8A-Timer,
347 mitophagy was inhibited by treating hiPSC-derived astrocytes transduced with COX8A-Timer with
348 the V-ATPase inhibitor bafilomycinA1 (BafA1). BafA1 treatment led to a significant increase in the
349 ratio of red-fluorescent mitochondria over green-fluorescent mitochondria compared to vehicle
350 control astrocytes (unpaired t-test, $p < 0.0001$; **Fig. 5C, D**). Since mitochondrial degradation and
351 turnover occur primarily through mitophagy, inhibition of mitophagy and mitochondrial recycling
352 via BafA1 treatment results in a predicted increase in longer-lived mitochondria.

353 Because PRKN is directly involved in mitophagy, and we observed impaired retrograde
354 mitochondrial transport in *PRKN*$^{-/-}$ neurons, we wanted to measure changes in mitochondrial
355 turnover in human *PRKN*$^{-/-}$ cells. We transduced wild-type (*PRKN*$^{+/+}$) and *PRKN* knockout *(PRKN*$^{-}$
356 $^{/-}$) hiPSC-derived astrocytes with GEM-SCOPe COX8A-Timer. The ratio of red-fluorescent signal
357 over green-fluorescent signal significantly increased in *PRKN*$^{-/-}$ astrocytes compared to *PRKN*$^{+/+}$
358 astrocytes (unpaired t-test, $p = 0.026$, **Fig. 5E, F**). When broken down by individual channel, there
359 was no change in the green fluorescence (2-way ANOVA with Sidak correction, p-adj = 0.1288,
360 **Fig. 5G**), indicating no change in mitochondrial biogenesis. The increase in red to green ratio was
361 driven by a significant increase in red-fluorescent signal (2-way ANOVA with Sidak correction, p-
362 adj = 0.0005, **Fig. 5G**), which is in concordance with an accumulation of older mitochondria due
363 to a failure to properly degrade mitochondria in the absence of PRKN. This observation is
364 supported in a Parkin-knockout mouse that showed a subtle increase in the protein half-life, and
365 therefore reduced protein turnover, of the subunits of the electron transport chain compared to
366 wild-type mice[85].

367 An expected consequence of impaired mitochondrial recycling is an accumulation of damaged
368 mitochondria and an increase in mitochondria-associated reactive oxygen species (ROS) from
369 inefficient cellular respiration. To measure reactive oxygen levels in live astrocytes, we introduced

370 GRX1-roGFP2, an established fluorophore for measuring ROS, into GEM-SCOPe[25]. GRX1-
371 roGFP2 is a fusion protein between GRX1 and roGFP2. When GRX1 is oxidized by glutathione,
372 it can subsequently oxidize roGFP2. Oxidized roGFP2 shifts its emission spectrum from green
373 fluorescence to blue fluorescence (**Fig. 6A**)[25,86]. Thus, the ratio of green to blue fluorescence is
374 an indicator of glutathione oxidation state. When GRX1-roGFP2 is further coupled with a
375 mitochondrial localization sequence, we can measure the oxidative stress of the mitochondria.

376 This construct was available as a retroviral vector using the signal sequence from *Neurospora*
377 *crassa* ATP synthase protein 9[25]. When we cloned it into the FUW lentivirus backbone, we decided
378 to keep that localization sequence rather than replace it with the signal sequence for COX8A used
379 in the other GEM-SCOPe mitochondria-localized fluorophores (**Fig. 6B**). To validate GEM-SCOPe
380 GRX1-roGFP2 was working as expected, hiPSC-derived astrocytes transduced with mito-GRX1-
381 roGFP2 were treated with BafA1 to induce oxidative stress[87]. Astrocytes treated with BafA1 had
382 a significant decrease in the ratio of green fluorescence to blue fluorescence when compared to
383 vehicle (DMSO) treated astrocytes (unpaired t-test, $p < 0.0001$, **Fig. 6C, D**). The effect is driven
384 by a significant increase specifically in blue fluorescence (2-way ANOVA with Sidak correction, p-
385 adj < 0.0001, **Fig. 6E**) while the green fluorescence remained unchanged (2-way ANOVA with
386 Sidak correction, p-adj = 0.99, **Fig. 6E**). The increase in blue fluorescence is due to an increase
387 in roGFP2 oxidation, which is indicative of an increase in glutathione oxidation and the presence
388 of reactive oxygen species. Thus, GEM-SCOPe-mito-GRX1-roGFP can be used to monitor
389 glutathione reduction potential and how cells respond to reactive oxygen stress.

390 Because astrocytes play important metabolically supportive roles in the CNS and we observed
391 PRKN-related impairments to mitochondrial recycling with COX8A-Timer (**Fig. 5E-G**), we wanted
392 to understand if PRKN deficiency has effects on ROS production in astrocytes. We transduced
393 *PRKN*$^{+/+}$ and *PRKN*$^{-/-}$ astrocytes with mito-GRX1-roGFP2 lentivirus. Without introducing any
394 additional chemical mitochondrial stressors, we observed a significant reduction in the ratio of

395 green-fluorescence signal to blue-fluorescence signal in *PRKN*$^{-/-}$ compared to *PRKN*$^{+/+}$ astrocytes
396 (1-way ANOVA with Tukey's HSD, p = 0.0003; **Fig. 6F, G**). This is indicative of an increase in ROS
397 in *PRKN*$^{-/-}$ astrocytes which correlates with our other observation of decreased mitochondrial
398 turnover in the same cells. We reintroduced the *PRKN* coding sequence into *PRKN*$^{-/-}$ astrocytes
399 via lentivirus (**Fig. S3B**), and found the ratio of green to blue fluorescence increased to levels
400 comparable to *PRKN*$^{+/+}$ astrocytes (1-way ANOVA with Tukey's HSD, p = 0.401); **Fig. 6F, G**),
401 confirming that the increase in ROS observed in *PRKN*$^{-/-}$ astrocytes was due to the loss of *PRKN*.
402 It has been previously demonstrated that *PRKN*$^{-/-}$ hiPSC-derived dopaminergic neurons show
403 increased cellular ROS[15] and *PRKN*$^{-/-}$ mice have decreased antioxidant capabilities and increased
404 ROS-related protein and lipid damage[88]. By introducing fluorophore-biosensors into our lentiviral
405 catalog, we were able to expand the phenotypes we can observe in live cells to measure changes
406 in the intracellular environment in response to chemical and genetic perturbations.

407

408 # Discussion

409 Here, we developed and validated GEM-SCOPe (Genetically Engineered, Modular, SubCellular
410 Organelle Probes), a collection of subcellularly targeted fluorophores encoded in a lentiviral
411 backbone. By exploiting the modular design of the constructs, we easily cloned fluorophores with
412 different excitation/emission spectra specified to localize to the nucleus, lysosomes, or
413 mitochondria. We demonstrated that these fluorophores specifically localize to the desired
414 organelle and can quantitatively assess cellular responses to chemical perturbations. Finally, we
415 applied GEM-SCOPe to human *PRKN*-knockout astrocytes and neurons, which revealed
416 widespread perturbations to cellular proliferation, lysosomal distribution, and mitochondrial
417 dynamics, providing new insights into PD pathogenesis.

418 Gliosis has been widely reported in human post-mortem brain studies of patients with *PRKN* loss-
419 of-function mutations[89-92]. Similar pro-inflammatory phenotypes have also been observed in
420 mouse models and stem-cell-derived glial models of PRKN deficiency[93,94]. However, there is still
421 a limited understanding of how genetic mutations related to PD modify astrocytes and their role
422 in neurodegeneration. We used GEM-SCOPe to investigate cellular, mitochondrial, and lysosomal
423 dynamics in astrocytes lacking functional PRKN protein. Using nucleus-localized fluorophores,
424 we show that *PRKN* knockout human astrocytes have increased cellular proliferation compared
425 to isogenic, wild-type astrocytes. LAMP1-localized fluorophores revealed that lysosomes in *PRKN*
426 knockout astrocytes are distributed further from the perinuclear nuclear area. Finally, a variety of
427 mitochondria-localized fluorophores revealed that *PRKN* knockout astrocytes have impaired
428 mitochondrial transport, decreased mitochondrial turnover, increased reactive oxygen species,
429 and oxidized glutathione. One limitation to the *PRKN* knockout model is the genetic variability that
430 can arise from culturing cells in vitro. While additional experiments must be done to support these
431 findings, our goal was to demonstrate the utility and efficacy of GEM-SCOPe to detect measurable
432 genetically mediated differences in cell models. GEM-SCOPe highlights that there is extensive
433 dysregulation and disruption to normal organelle dynamics in human *PRKN* astrocytes that
434 warrants further investigation.

435 GEM-SCOPe was developed in a 3rd generation lentiviral system. We selected this delivery
436 system because 1) lentiviruses are safe to produce; 2) they infect both dividing and non-dividing
437 cells; and 3) they can be used to develop stable cell lines. 3rd generation lentiviral systems are
438 replication-incompetent, so cells that are transduced with lentivirus cannot produce more viral
439 particles. Only the transfer plasmid, which contains the insert of interest, can be integrated into
440 the host genome; the other plasmids that encode lentiviral structural and envelope genes do not
441 integrate into the host genome, preventing viral replication. Most lentiviruses are produced with
442 VSV-G (Vesicular stomatitis virus G glycoprotein) as the envelope protein, as it provides broad

443 tropism and enables high transduction efficiency in a wide variety of cell types[95]. Finally, GEM-
444 SCOPe lentiviruses were developed with the option to include an antibiotic-resistance gene (**Fig.**
445 **1A**), which can be used to establish stable cell lines that have incorporated the lentiviral load.

446 Although lentiviruses provide a lot of flexibility and safety when delivering genetic information,
447 they also possess some limitations. Lentiviruses have an ideal plasmid size of 9-10kb, and viral
448 titer can decrease if plasmids exceed this size[96]. The H2B-mTagBFP2, H2B-mCherry, and H2B-
449 Emerald lentiviruses (**Fig. 1, 2**) are about 11kb each and transduced hiPSC-derived astrocytes
450 with about 90% efficiency. Coupled with the puromycin resistance that was also included in this
451 construct, we were still able to generate a population with 100% viral transduction despite the size
452 limitation. Another drawback of lentiviral gene delivery is that inserts often integrate into actively
453 transcribed loci[97]. Differentiation of hiPSCs into specific cell types requires extensive chromatin
454 remodeling, and genomic sequences integrated via lentivirus can often be silenced in this
455 process. In the case where hiPSCs must be transduced before differentiation, antibiotic selection
456 during differentiation can select for cells that have integrated the viral load into a genomic region
457 that is not silenced. The final drawback of lentiviral gene delivery is that fluorescence intensity is
458 dependent on the viral copy number in each cell and cannot be used as a readout for organelle
459 abundance. Rather, we need to use measurements like distribution, size, and ratios of different
460 emissions within the same cell. This is not just a limitation of lentiviral gene delivery but of other
461 viral and non-viral delivery systems.

462 In this study, we focused on PD and specifically the alterations to astrocytes with *PRKN* mutations.
463 However, alterations in proliferation, mitochondria, and lysosomes are by no means unique to
464 *PRKN* or PD. Many reviews cover the extensive roles of mitochondria and lysosomes in health
465 and disease[98-101]. GEM-SCOPe can be applied to countless cell types and *in vitro* disease models
466 to investigate subcellular dynamics in the development and progression of a variety of diseases,
467 beyond neurodegeneration. Due to its modular design, GEM-SCOPe can be expanded and

468 molded by research groups to meet specific needs. Different targeting sequences can be
469 integrated to localize fluorophores to relevant subcellular compartments. New fluorophores and
470 biosensors are always being developed to measure additional intracellular conditions. By applying
471 GEM-SCOPe to disease models, we will be able to better understand how cells are disrupted
472 over the course of disease progression, providing insight for future therapeutic targets.

473

474 Resource Availability

475 Lead contact

476 Further information and requests for resources and reagents should be directed to and will be
477 fulfilled by the lead contact, Joel W. Blanchard (joel.blanchard@mssm.edu).

478 Materials availability

479 All plasmids generated in this study have been deposited to Addgene (**Table S1**).

480 Data and code availability

481 • Raw data from all Figures and Supplemental Figures is available on Mendeley (DOI:
482 10.17632/fmxdjgrjw5.1)
483 • This paper does not report original code.
484 • Any additional information required to reanalyze the data reported in this paper is available
485 from the lead contact upon request.

486

487 # Limitations of Study

488 In this study, we focused on *PRKN*$^{-/-}$ astrocyte phenotypes grown in monocultures. I future
489 studies, it would be crucial to examine astrocyte phenotypes in a more complex multi-culture
490 system, as responses to inputs from other cell types may affect astrocyte behavior in a disease-
491 relevant manner. Furthermore, we only used a *PRKN*$^{-/-}$ cell line generated from one human, male
492 donor. In future studies, it would be important to validate our findings in other iPSC lines,
493 especially from both male and female donors, to confirm the relevance of observed phenotypes
494 across cell lines with different genetic backgrounds.

495 # Acknowledgements

496 The authors thank Deanna Benson for discussions on mitochondrial transport and kymograph
497 analysis. We thank the Microscopy CoRE at Icahn School of Medicine for providing access to the
498 Leica DMi8 and Thermo Scientific CX7 High Content Screening Platform, as well as training and
499 technical expertise for using these microscopes.

500 This work has been funded in part with federal funds from NASA under contract
501 #80ARC022CA004 titled "Identification of Biomarkers and Pathological Mechanisms via
502 Longitudinal Analysis of Neurological and Cerebrovascular Responses to Neurotoxic Stress
503 Using a Multi-cellular Integrated Model of the Human Brain." This research was funded in whole
504 or in part by Aligning Science Across Parkinson's (ASAP-024297) through the Michael J. Fox
505 Foundation for Parkinson's Research (MJFF). For open access, the authors have applied a CC
506 BY public copyright license to all Author Accepted Manuscripts arising from this submission. This
507 work was also supported by funding from the NIH/NINDS (R01NS114239 and UH3NS115064),
508 and the CureAlz Fund. C.G. was supported by funding from the NIH/NIA (T32AG04968) and

NIH/NINDS (F31NS13090), and L.S. was supported by the Training Program in Stem Cell Biology fellowship from the New York State Department of Health (NYSTEM-C32561GG).

Author Contributions

Conceptualization, C.G., T.A., and J.W.B.; Methodology, C.G., L.S., and T.A.; Validation, C.G.; Formal Analysis, C.G.; Investigation, C.G., T.K., L.S., and A.S.; Resources, C.G., T.K., L.S., and B.R.S.; Writing – Original Draft, C.G. and J.W.B.; Writing – Review & Editing, C.G., L.S., B.R.S., and J.W.B.; Visualization, C.G.; Funding Acquisition, T.A. and J.W.B.

Declaration of Interests

The authors declare no competing interests.

Figure Legends

Fig. 1: A toolbox of lentiviral plasmids developed and validated for subcellular localization of fluorophores (A) Schematic of lentiviral plasmids highlighting the combinatorial power of the toolbox components. Generated using BioRender **(B)** Schematic demonstrating the cloning strategies used to generate the constructs used in this study as well as any future constructs. Generated using BioRender **(C)** Representative images of subcellular localization validation with available dyes in hiPSC-derived astrocytes and Mander's co-efficient for overlap of the genetically encoded fluorophore with the dye. Bars represent mean values and error bars represent standard

529 deviation. Top: H2B-mTagBFP2 and DRAQ5 (n = 3; each replicate is an average over 16 images);
530 Middle: LAMP1-mCherry and LysoTracker Deep Red; nuclei stained with Hoechst33342 (n = 4;
531 each replicate is an average over 4 images); Bottom: COX8A-Emerald and MitoTracker Deep
532 Red; nuclei stained with Hoechst33342 (n = 3, each replicate is an average over 36 images).
533 Scale bars = 50 μm **(D)** Representative images of combinatorial applications of GEM-SCOPe.
534 Top: Cell expressing LAMP1-Emerald and COX8A-mCherry. Bottom: cell expression LAMP1-
535 mCherry and COX8A-Emerald. Nuclei were stained with DRAQ5. Scale bars = 50 μm. See also
536 Figure S1 and Table S1.

537 **Fig. 2: Nucleus-localized fluorophores offer improvements over available stains for**
538 **multiday imaging (A)** Schematic of the lentiviral construct localizing mTagBFP2 to the nucleus
539 with an H2B fusion protein and antibiotic resistance to puromycin used in the following panels **(B)**
540 Representative images of H2B-mTagBFP2 and DRAQ5 nuclear stain 1 hour (top) and 24 hours
541 (bottom) after adding DRAQ5 to the cell cultures. **(C)** Quantification of the percent of stain
542 localized to the nuclear area versus the cytoplasm 1 hour and 24 hours after adding DRAQ5 to
543 cell cultures. The central bar represents the mean and the error bars represent the standard
544 deviation (2-way ANOVA with Tukey's HSD; n = 3 per time point; each replicate is an average
545 over 36 images) **(D)** Schematic of the lentiviral construct localizing Emerald or mCherry to the
546 nucleus with an H2B fusion protein and antibiotic resistance to puromycin used in the following
547 panels **(E)** Representative images of nuclei from *PRKN*$^{+/+}$ astrocytes, labeled with H2B-Emerald,
548 and *PRKN* $^{-/-}$ astrocytes, labeled with H2B-mCherry, cultured together during a proliferation assay.
549 Images were taken 24 hours (top) after seeding and 72 hours (bottom) after seeding **(F)**
550 Quantification of number of *PRKN*$^{+/+}$ and *PRKN*$^{-/-}$ nuclei per image field 24 hours and 72 hours
551 after seeding. Dots represent mean values and error bars represent standard deviation (2-way
552 ANOVA with Tukey's HSD; n = 3 per time point; each replicate is an average over 25 images).
553 Scale bars = 50 μm. All images were acquired on the CX7 HCS platform with a 20x objective lens.

554 For all graphs, * p< 0.05, ** p < 0.01, *** p < 0.001, **** < 0.0001. See also Figure S2 and Figure
555 S3.

556 **Fig. 3: Lysosome-localized fluorophores reveal changes in lysosomal distribution upon**
557 **chemical and genetic perturbation (A)** Schematic of the lentiviral constructs used in the
558 following panels localizing (top) mCherry to the lysosome with the 5' sequence of *LAMP1* and
559 (bottom) Emerald to the whole cell by not including a localization sequence. **(B)** Representative
560 images of astrocytes transduced with Emerald and LAMP1-mCherry lentiviruses and treated with
561 100 nM bafilomycin A1 (bottom) or a vehicle (DMSO; top). Nuclei were stained with
562 Hoechst33342. Far right: Output from CellProfiler showing the distribution Lamp1-mCherry signal
563 as a fraction of signal in each bin. Darker blue indicates a higher fraction of signal in that bin.
564 Scale bars = 50 µm. **(C)** Quantification of lysosomal number per cell (left), average vesicle area
565 (middle) and fraction of perinuclear lysosomes (right) using Lamp1-mCherry signal in vehicle
566 (DMSO) and bafilomycin A1 (100 nM) treated astrocytes. Emerald was used to determine cell
567 boundaries. Central bars represent mean and error bars represent standard deviation (unpaired
568 t-tests; n = 4; each replicate is an average over 10 images). **(D)** Representative images of *PRKN*$^{+/+}$
569 (top) and *PRKN*$^{-/-}$ (bottom) astrocytes transduced with cytoplasmic Emerald and LAMP1-mCherry
570 lentiviruses. Nuclei were stained with Hoechst33342. Far right: Output from CellProfiler showing
571 the distribution Lamp1-mCherry signal as a fraction of signal in each bin. Darker blue indicates a
572 higher fraction of signal in that bin. Scale bars = 25 µm. (**E**) Quantification of Lamp1-mCherry
573 signal in *PRKN*$^{+/+}$ and *PRKN*$^{-/-}$ astrocytes to measure lysosomal number per cell (left), average
574 vesicle area (middle) and fraction of perinuclear lysosomes (right). Emerald fluorescence was
575 used to determine cell boundaries. Central bars represent mean and error bars represent
576 standard deviation (unpaired t-tests; n = 6; each replicate is an average over 7 images). All images
577 were acquired on a Nikon Ti2E AX R confocal microscope with a 20x objective lens and 6x optical
578 zoom. For all graphs, * p< 0.05, ** p < 0.01, *** p < 0.001, **** < 0.0001.

579 **Fig. 4: Mitochondria-localized fluorophores resolve changes in mitochondrial network**
580 **dynamics (A)** Schematic of the lentiviral construct used in the following panels localizing Emerald
581 to the mitochondria with the targeting sequence of COX8A. **(B)** Representative images of
582 astrocytes transduced with COX8A-Emerald and treated with a vehicle (DMSO; top) or 2 uM
583 oligomycin (bottom). Nuclei were stained with Hoechst33342. High magnification images (far
584 right) highlight the changes to the mitochondrial network upon oligomycin treatment. Scale bars
585 = 50 µm. **(C)** Quantification of mean mitochondrial area, mean mitochondrial branch length, and
586 mean aspect ratio upon oligomycin treatment. Central bars represent mean and error bars
587 represent standard deviation (1-way ANOVAs with Dunett's test; n = 3; each replicate is an
588 average over 36 images) **(D)** Representative images of mitochondria labeled with COX8A-
589 Emerald moving along *PRKN*$^{-/-}$ neuron axons in the anterograde (left) and retrograde (right)
590 directions. Scale bars = 5 µm. Images were taken on a Leica DMi8 microscope for 1 hour per field
591 **(E-F**). Quantification of mitochondrial run length (left) and run time (right) of COX8A-Emerald
592 labeled mitochondria in *PRKN*$^{+/+}$ and *PRKN*$^{-/-}$ dopaminergic neuron axons moving anterograde
593 (E) and retrograde (F) as determined by kymograph analysis (unpaired t-test or Welch's test;
594 average of n = 37.5 organoids for anterograde and 23.5 organoids for retrograde; each replicate
595 is an average over 1-3 fields). See also Figure S4. For all graphs, * $p < 0.05$, ** $p < 0.01$, *** $p <$
596 0.001, **** < 0.0001.

597 **Fig. 5: Timer fluorophore measures changes in subcellular mitochondrial turnover in**
598 ***PRKN*$^{-/-}$(A)** Schematic demonstrating how the fluorescent protein Timer works. Timer undergoes
599 a fluorescent shift from a green emission to a red emission overtime; analysis of Timer relies on
600 examining the ratio between the red and green emission. **(B)** Schematic of the lentiviral construct
601 used in the following panels localizing Timer to the mitochondria by using the targeting sequence
602 of COX8A. **(C)** Representative images of astrocytes transduced with COX8A-Timer and treated
603 with a vehicle (DMSO; top) or 100 nM bafilomycin A1 (bottom) for 24 hours. Images were acquired

604 with a 488-excitation line and a 594-excitation line. Far right: ratiometric representation of the red
605 channel divided by the green channel and pseudo colored so that orange, yellow and white
606 indicate more relative red emission and black and purple indicate more relative green emission.
607 Nuclei were stained with DRAQ5. Scale bars = 50 μm. **(D)** Quantification of the ratio of mean
608 intensity of emission from excitation with a 594nm laser to the mean intensity of emission from
609 excitation with a 488 nm laser in astrocytes expressing COX8A-Timer and treated with a vehicle
610 (DMSO) or 100 nM bafilomycin A1 for 24 hours. Central bars represent mean and error bars
611 represent standard deviation (unpaired t-test; n = 6; each replicate is an average over 25 images).
612 (**E**) Representative images of *PRKN*$^{+/+}$ and *PRKN*$^{-/-}$ astrocytes transduced with COX8A-Timer.
613 Images were acquired with a 488-excitation line and a 594-excitation line. Far right: ratiometric
614 representation of the red channel divided by the green channel and pseudo colored so that
615 orange, yellow and white indicate more relative red emission and black and purple indicate more
616 relative green emission. Nuclei were stained with DRAQ5. Scale bars = 50 μm. **(F)** Quantification
617 of the ratio of mean intensity of emission from excitation with a 594nm laser to the mean intensity
618 of emission from excitation with a 488 nm laser in *PRKN*$^{+/+}$ and *PRKN*$^{-/-}$ astrocytes expressing
619 COX8A-Timer. Central bars represent mean and error bars represent standard deviation (n = 3;
620 each replicate is an average over 25 images). **(G)** Quantification of mean intensity normalized by
621 nuclear area of green and red fluorescence in *PRKN*$^{+/+}$ and *PRKN*$^{-/-}$ astrocytes expressing
622 COX8A-Timer. Central bars represent mean and error bars represent standard deviation (2-way
623 ANOVA with Sidak correction; n = 3; each replicate is an average over 25 images). All images
624 were acquired on a CX7 HCS platform with a 20x objective lens. For all graphs, * $p < 0.05$, ** $p <$
625 0.01, *** $p < 0.001$, **** < 0.0001.

626 **Fig. 6: GRX1-roGFP2 fluorophore is used to quantify glutathione oxidation in chemical and**
627 **genetic models of oxidative stress (A)** Schematic demonstrating how the fluorescent protein
628 fusion Grx1-roGFP2 works. Oxidation of Grx1 upon the oxidation of glutathione results in the

629 eventual oxidation of roGFP2, shifting its emission spectrum from green to blue. **(B)** Schematic
630 of the lentiviral construct used in the following panels localizing Grx1-roGFP2 to the mitochondria.
631 This fluorophore was localized using atp-9 instead of COX8A. **(C)** Representative images of
632 astrocytes transduced with mito-GRX1-roGFP2 and treated with a vehicle (DMSO; top) or 100
633 nM bafilomycin A1 (bottom) for 24 hours. Images were acquired with a 405-excitation laser and a
634 488-excitation laser. Far right: ratiometric representation of the green channel divided by the blue
635 channel and then pseudo colored so that orange, yellow and white indicate more relative green
636 emission while black and purple represent more blue emission. Nuclei were stained with DRAQ5.
637 Scale bars = 50 μm. **(D)** Quantification of the ratio of mean intensity from 488-excitation to the
638 mean intensity from 405 excitation. In astrocytes expression mito-Grx1-roGFP2 and treated with
639 a vehicle or 100 nM bafilomycin A1. Central bars represent mean and error bars represent
640 standard deviation (unpaired t-test; n = 6; each replicate is an average over 25 images). **(E)**
641 Quantification of mean intensity normalized by nuclear area of blue and green fluorescence in
642 vehicle and bafilomycin A1 treated astrocytes expressing mito-Grx1-roGFP2. Central bars
643 represent mean and error bars represent standard deviation (n = 6; each replicate is an average
644 of 25 images). **(F)** Representative images of *PRKN*$^{+/+}$, *PRKN*$^{-/-}$, and *PRKN*$^{-/-}$ with *PRKN*-
645 overexpression astrocytes transduced with mito-Grx1-roGFP2. Images were acquired with a 405-
646 excitation laser and a 588-excitation laser. Far right: ratiometric representation of the green
647 channel divided by the blue channel and pseudo colored so that orange, yellow and white indicate
648 more relative green emission and black and purple indicate more relative blue emission. Nuclei
649 were stained with DRAQ5. Scale bars = 50 μm. **(G)** Quantification of the ratio of mean intensity
650 of emission from excitation with a 488nm laser to the mean intensity of emission from excitation
651 with a 405 nm laser in *PRKN*$^{+/+}$, *PRKN*$^{-/-}$, and *PRKN*$^{-/-}$ with *PRKN*-overexpression astrocytes
652 expressing mito-Grx1-roGFP2. Central bars represent mean and error bars represent standard
653 deviation (1-way ANOVA with Tukey's HSD; n = 6; each replicate is an average over 36 images).
654 For all graphs, * $p < 0.05$, ** $p < 0.01$, *** $p < 0.001$, **** < 0.0001. See also Figure S3.

655 **Fig. S1: GEM-SCOPe supports a diversity of modifications and applications (A)**
656 Representative images of astrocytes expressing COX8A-Emerald under the control of a
657 doxycycline inducible promoter. Astrocytes were treated with a vehicle (DMSO; top) or
658 doxycycline (bottom) for 72 hours. Nuclei were stained with Hoechst33342. **(B)** Representative
659 images of a mixed population of astrocytes with nuclei expressing different H2B-fusion
660 fluorophores. Astrocytes were transduced with a single lentivirus and then plated together. **(C)**
661 qPCR for endogenous *LAMP1* (left) and lentiviral *LAMP1* (right) on RNA from astrocytes
662 transduced with a virus localized to the lysosome (LAMP1-mCherry) or a virus not localized to the
663 lysosome (COX8A-Emerald). Endogenous *LAMP1* qPCR primers were designed to amplify a
664 sequence of *LAMP1* that is not included in the lentivirus and lentiviral *LAMP1* qPCR primers were
665 designed to amplify the signal sequence of *LAMP1* and the beginning of the mCherry sequence.
666 Bars represent mean and error bars represent standard deviation (n = 3 independent
667 transductions). Statistical differences were determined by unpaired t-test; (left) p = 0.07; (right) p
668 = 0.002. **(D)** Schematic of the lentiviral construct used in the following panels localizing Lemon,
669 a pH responsive fluorophore, to the mitochondria with the targeting sequence of COX8A. Lemon
670 undergoes Forster Resonance Energy Transfer (FRET) under alkaline conditions. **(E)**
671 Representative images and quantification of astrocytes transduced with COX8A-Lemon and
672 treated with a vehicle (DMSO; top) or 2 μM oligomycin (bottom) for 24 hours. Images were
673 acquired with a 455nm-excitation laser and a 515-excitation laser. Far right: ratiometric
674 representation of the emission in the yellow channel divided by the emission in the cyan channel
675 and then pseudo colored so that orange, yellow and white indicate more relative yellow emission
676 (more alkaline) while black and purple represent more cyan emission (more acidic). Nuclei were
677 stained with DRAQ5. Central bars represent mean and error bars represent standard deviation
678 (n = 3; each replicate is an average 36 images). Scale bars = 50 μm. For all graphs, * p< 0.05, **
679 p < 0.01, *** p < 0.001, **** < 0.0001.

680 **Fig. S2: Astrocyte proliferation is activated by FBS and inhibited by MG-132 (A)**
681 Representative images of astrocytes transduced with H2B-Emerald lentivirus after 0 hrs (top) or
682 48 hrs (bottom) of treatment with a vehicle (DMSO; left), 10% fetal bovine serum (FBS; middle),
683 or MG132 (right). Scale bars = 50 μm. **(B)** Quantification of number of H2B-Emerald nuclei per
684 image field 0 hours and 48 hours after treatment. Dots represent mean values and error bars
685 represent standard deviation (n = 6 (n = 3 for MG-132 treatment) per time point; each replicate is
686 an average over 25 images). Scale bars = 50 μm. All images were acquired on the CX7 HCS
687 platform with a 20x objective lens. For all graphs, * $p< 0.05$, ** $p < 0.01$, *** $p < 0.001$, **** <
688 0.0001.

689 **Fig. S3: *PRKN* knockout and overexpression (A)** Sequencing alignment of *PRKN*$^{-/-}$ astrocytes
690 with the *PRKN* coding sequence showing a 62bp deletion in exon 3 **(B)** qPCR for *PRKN* in
691 *PRKN*$^{+/+}$, *PRKN*$^{-/-}$, and *PRKN*$^{-/-}$ with *PRKN*-overexpression. qPCR primers were designed to
692 amplify the region deleted in the *PRKN*$^{-/-}$ cells. Bars represent mean and error bars represent
693 standard deviation (1-way ANOVA with Tukey's HSD; *PRKN*$^{+/+}$ vs *PRKN* knock-in: $p = 0.0004$;
694 *PRKN*$^{-/-}$ vs *PRKN* knock-in: $p = 0.0004$; n = 3 independent transductions). For all graphs, * $p<$
695 0.05, ** $p < 0.01$, *** $p < 0.001$, **** < 0.0001.

696 **Fig. S4: Mitochondrial fragmentation exhibits a dose dependent response to oligomycin-**
697 **induced stress (A)** Representative images of astrocytes transduced with COX8A-Emerald and
698 treated with a vehicle (DMSO), 1μM, 2 μM, or 5 μM oligomycin for 4 hours. Nuclei were stained
699 with Hoechst33342. Scale bars = 50 μm **(B)** Quantification of mitochondrial features indicative of
700 mitochondrial network fragmentation: mean area, perimeter, aspect ratio, number of branches,
701 branch length, and number of branch endpoints. Central bars represent mean and error bars
702 represent standard deviation (1-Way ANOVAs with Dunnett's test; n = 3; each replicate is an
703 average over 36 images). For all graphs, * $p< 0.05$, ** $p < 0.01$, *** $p < 0.001$, **** < 0.0001.

704

705 # STAR Methods

706 ## Experimental model and study participant details

707 The human cell lines used in this study are detailed in the key resources table as well as below.
708 HEK293FT (RRID: CVCL_6911, fetal kidney origin, female sex) were maintained in DMEM (Gibco
709 10566) supplemented with 10% bovine calf serum (Cytiva SH30073) at 37 °C in a 5% CO2
710 incubator. Cells were passaged every 4-5 days, when they reached 90% confluency.

711 H1(WA01) hESCs (male), BJ-SiPS-D iPSCs (male), and AG09173 iPSCs (female) were
712 maintained in StemFlex medium (Gibco A3349401) at 37 °C in a 5% CO2 incubator. Cells were
713 passaged every 3-4 days, when they reached 90% confluency. WA01 *PRKN*$^{-/-}$ isogenic lines were
714 previously generated and validated in Ahfeldt et. al, 2020.[15] WA01 astrocytes were used for all
715 PRKN-genotype dependent experiments. BJ-SiPS-D and AG09173 were used for organelle
716 localization validation and chemical perturbation validation. All iPSC lines have undergone quality
717 control analysis including tests for pluripotency, genomic instability, sterility, and cell line identity,
718 and routine mycoplasma testing prior to experimentation.

719 ## Method Details

720 Detailed methods are available at dx.doi.org/10.17504/protocols.io.4r3l2pj4pg1y/v1

721 ### Molecular cloning

722 All vectors were derived from pFUW (Addgene plasmid #14882). pFUW was linearized using
723 NheI-HF (NEB R3131) and BamHI-HF (NEB R3136) per manufacturer's protocol, and the desired
724 fragment was gel-purified (Macherey-Nagel 740609). Components of the insert were PCR
725 amplified using Q5-Hot Start DNA Polymerase (NEB M0493) per manufacturer's
726 recommendations. Fluorophores were amplified from commercially available plasmids (see
727 Resource Table for complete list) and localization sequences were amplified from cDNA. Primers

728 were designed using the NEBuilder Assembly Tool (nebuilder.neb.com) to add 5' and 3'
729 sequences that make the fragments compatible for Gibson assembly and ordered from IDT
730 (Integrated DNA Technologies). Gibson reactions were set up with NEBuilder HiFi DNA Assembly
731 Master Mix (NEB E2621), 50ng of linearized backbone, and 3-fold molar excess of each PCR
732 fragment. For fragments less than 200bp, 5-fold molar excess was used. Reactions were
733 incubated at 50°C for 60 minutes. The Gibson product was transformed in 10-beta competent *E.*
734 *coli* (NEB C3019) grown on LB Agar plates with 100ug/mL ampicillin. Plasmids from single clones
735 were isolated via miniprep (Macherey-Nagel 740499) and sequenced to confirm successful
736 cloning.

737

738 Lentivirus Production

739 Lentivirus was produced by transfection of HEK293T cells as adapted from Dull et al. 1998 [102].
740 HEK293T cells were grown in Dulbecco's Modified Eagle Medium (DMEM; Gibco 11965092) with
741 10% bovine calf serum (Cytiva SH30073) at 37 °C in a 5% CO_2 incubator. The day before
742 transfection, ~10^7 cells were plated per 15cm dish coated in 0.1% gelatin. Media was changed
743 just prior to transfection. For one 15cm dish, 22.5ug of transfer vector was combined with 14.7ug
744 of pMDLg/pRRE (Addgene plasmid #12251), 5.7ug of pRSV.Rev (Addgene plasmid #12253), and
745 7.9ug of pMD2.G (Addgene plasmid #12259) in a 15mL conical tube. The plasmid mixture was
746 added to 1mL of 278 uM $CaCl_2$ (Sigma C1016) and mixed thoroughly before adding 1mL of 2x
747 BBS solution [280 mM NaCl (Fisher Scientific S271-1), 50 mM BES (Millipore 391334), 1.5mM
748 Na_2HPO_4 (Sigma S5136); pH = 6.95] dropwise. Tubes were mixed by inversion, incubated at room
749 temperature for 1 min, and then added dropwise to HEK293T dish. Cell culture media was
750 changed after 16-24 h. Conditioned media was then collected every 24 h for 2 days; conditioned
751 media from the same plate was combined over the two collections. Conditioned media was
752 centrifuged at 2000 x g for 10 minutes to pellet debris and filtered through 0.22-um-pore-size PES

753 filter (Millipore SCGP00525). To concentrate virus, filtered media was incubated with PEG 8000
754 (Sigma P2139) and NaCl, at a final concentration of 5% and 0.15M respectively, overnight at 4°C,
755 then centrifuged at 3000 x g for 20 min. The pellet was resuspended in DMEM/F12 with GlutaMAX
756 (Gibco 10565018) to 1% of the original supernatant volume. The concentrated virus was stored
757 in aliquots at -80°C.

758

759 Midbrain Organoid and Astrocyte Differentiation

760 hiPSC-derived astrocytes were extracted from 100-day-old midbrain organoids as described in
761 Sarrafha et al 2021 and Parfitt et al 2024 [81,103]. A detailed protocol can be found at
762 https://doi.org/10.1016/j.xpro.2021.100463. In short, hiPSCs were cultured in StemFlex medium
763 (Gibco A3349401) at 37 °C in a 5% CO_2 incubator. hiPSCs were seeded into 125-mL spinner
764 flasks (Corning 3152) and allowed to self-aggregate in StemFlex (Gibco A3349401)
765 supplemented with 10 μM Y-27632 (Tocris 1254) and 1% Penicillin-Streptomycin (Gibco
766 15140122). Once aggregates were between 300 μm and 500 μm, differentiation was initiated by
767 dual-SMAD inhibition with 10 μM SB431542 (Stemgent 04-0010), 100nM LDN193189 (Tocris
768 6053), 1x B27 without Vitamin A (Gibco 12587010) and 1x N2 (Gibco 17502048) in DMEM-F12
769 with GlutaMAX (Gibco 10565018). Midbrain patterning was achieved with the addition of 3 μM
770 CHIR99021 (Tocris 4423), 2 μM purmorphamine (Stemcell 72204), and 1 μM SAG (Cayman
771 11914) starting 4 days after neural induction. After patterning, media was changed to DMEM/F12
772 with GlutaMAX, supplemented with 1x N2, 1x B27 without Vitamin A, 20 ng/mL GDNF (Peprotech
773 450-10), 20 ng/mL BDNF (Peprotech 450-02), 200 μM L-ascorbic acid (Fisher Scientific BP351),
774 100 μM dibutyryl cAMP (Biogems 1698950), and 10 μM DAPT (Cayman 13197). After 35 days,
775 organoids were transferred to ultra-low attachment plates (Corning 3516), with about 5 organoids
776 per mL of media and cultured in DMEM/F12 with GlutaMAX supplemented with 1x N2, 1x B27
777 without Vitamin A, 10 ng/mL GDNF, 10 ng/mL BDNF, and 200 μM ascorbic acid.

778 Astrocytes were extracted from midbrain organoids starting at day 100. Organoids were gently
779 dissociated in a trypsin enzyme solution (TrypLE Select, Gibco 12563011) using a glass pipette
780 to break up organoids into large chunks. The organoid chunks from 5-10 organoids were placed
781 on 15cm dishes coated with 0.1% gelatin and maintained in Astrocyte Medium (AM; ScienCell
782 #1801). Astrocytes were allowed to grow out of the organoid chunks until the plate was confluent
783 (about 1 week). At this point, astrocytes can be cryopreserved. Astrocytes were maintained in AM
784 and switched to experimental media [1:1 DMEM/F-12:Neurobasal (Gibco 21103049), 1x B27
785 without Vitamin A, 1x N2, 1x MEM-Non-Essential Amino Acids (Gibco 11140050), 1x GlutaMAX
786 (Gibco 35050061), 10 ng/mL CNTF (Peprotech 450-13)] 2-3 days before imaging.

787

788 Astrocyte Viral Transduction

789 iPSC-derived astrocytes were transduced during regular passaging. In short, astrocytes were
790 lifted, spun down, resuspended in AM media, and divided into 1.5mL microcentrifuge tubes,
791 depending on the desired split ratio and number of transductions. The virus was added to the cell
792 suspension and incubated for 5-10 minutes before plating the mixture. Media was topped off such
793 that the final dilution of the virus in media was 1:50. Depending on the viral titer, this dilution
794 sometimes increased or decreased. Astrocytes can also be transduced without passage by
795 adding the virus directly to the media. Media is changed after 24 hours. Antibiotics were added to
796 the media, if relevant, starting at least 3 days after transduction.

797

798 MitoTracker and LysoTracker

799 For MitoTracker staining, astrocytes were incubated with 100 nM of MitoTracker DeepRed
800 (Thermo Scientific M22425) for 30 min at 37 °C. For LysoTracker staining, astrocytes were

801 incubated 100 nM of LysoTracker DeepRed (Thermo Scientific L12492) for 5 min at 37 °C. Cells
802 were then washed twice with PBS before incubation with Hoechst 33342 (Thermo Scientific
803 62249).

804

805 qPCR

806 RNA was extracted from samples using TRIzol (Invitrogen 15596018) and an RNA extraction kit
807 following the manufacturer's recommended protocol (Zymo R2062). RNA concentration and purity
808 were measured on a spectrophotometer. cDNA was produced from 1 ug of RNA per sample, using
809 Maxima H Minus Reverse Transcriptase (Thermo Scientific EP0752) and following the
810 manufacturer's recommendations. qPCR reactions were prepared in a 384-well plate (Applied
811 Biosystems 4309849) with 1:10 dilution of cDNA, 2x PowerUp SYBR Green Master Mix (Applied
812 Biosystems A25741) and 1 μM each of forward and reverse primers. qPCRs were run on
813 QuantStudio 7 (Applied Biosystems 4485701) and analyzed using the ΔΔCt method, normalized
814 to *ACTB* and *S18* rRNA. The primers can be found in the key resources table.

815

816 Live Cell Imaging

817 In general, astrocytes were seeded at 10 x 10^3 cells per well of a 96-well plate with a cover glass
818 thickness polystyrene bottom (Greiner 655090) coated in 0.1% gelatin 3-5 days before imaging.
819 Proliferation assays were seeded at 8 x 10^3 cells per well and started 1 day after seeding. Before
820 imaging, cells were incubated with Hoechst 33342 (Thermo Scientific 62249) or DRAQ5 (Thermo
821 Scientific 52251) for 10 minutes.

822 Wide-field live cell imaging was performed using the Thermo Scientific CX7 High Content
823 Screening Platform with 20x and 40x objective lenses (LUCPLFLN20x and LUCPLFLN40x). The

824 microscope was equipped with an incubation unit that maintained temperature, CO_2, and humidity
825 during image acquisition. Confocal images were acquired on a Nikon Ti2E AX R confocal
826 microscope with a 20x objective lens (PLAN APO λD 20x) and 6x optical zoom. Each well was
827 imaged in 5 (confocal) or 25-36 (widefield) different areas, with the average of those images
828 represented as a single data point.

829

830 ImageJ Image Analysis

831 Nuclear Proliferation: Nuclear proliferation was quantified by converting images to a binary based
832 on a threshold and then using 'Analyze Particles' to obtain a count for the number of nuclei in a
833 field. The same threshold and parameters were kept for all time points.

834 Mitochondrial Fragmentation: Mitochondrial fragmentation was measured using the ImageJ
835 plugin, Mitochondrial Analyzer [104]. For thresholding, the "Block Size" was set to 1.45 microns and
836 the "C-Value" was set to 5.

837 Ratiometric Quantification: Ratiometric quantifications for roGFP2, Timer, and Lemon were
838 achieved by measuring the mean grey value in both channels of interest. The values for each
839 channel were then divided to generate the ratio of relative intensity between the two channels.

840 Kymograph Analysis: Kymograph analysis of mitochondrial movement was achieved using the
841 Image J plugins KymographClear 2.0 and KymographDirect [105]. KymographClear 2.0 was used
842 to trace mitochondrial trajectories and generate kymographs from which stationary and motile
843 mitochondria were identified. KymographDirect was then used to extract quantitative information
844 from the trajectories of the motile mitochondria.

845

Cell Profiler Image Analysis [72,106]

Subcellular Co-localization: For nuclear co-localization, nuclei in the genetically encoded fluorophore channel and the DRAQ5 channel were identified, and nuclei from cells that were not transduced were filtered out. For lysosomal and mitochondrial co-localization, propagation from the nuclear stain was used to identify cell bodies. Cells were filtered to only analyze those with lentivirus signal within the cell body. Co-localization was reported as the Mander's coefficient indicating the overlap of the genetically encoded fluorophore with the commercially available stain.

Lysosomal Distribution: Cells were defined by nuclei and full cell fluorophore signal. Lamp1-mCherry signal was assigned to the cell body with which it overlapped. Only cells that were successfully transduced were included in the analysis. The distribution of the Lamp1-mCherry signal was calculated using the "MeasureObjectIntensityDistribution" with two bins generated for each cell using the nuclei as the center of the cell. Bins were scaled such that the inner bin (perinuclear) was always the same percentage of total cell area regardless of cell size.

Quantification and statistical analysis

All experiments were conducted with 3-6 replicates. All quantifications were represented as mean ± standard deviation, except for the violin plots of the kymograph analysis. Details on data visualization, sample size, and images per replicate are included in figure captions. Details on statistical tests and significance are included in the text. For all statistical tests, $*p < 0.05$, $**p < 0.01$, $***p < 0.001$, $****p < 0.0001$. All statistical tests were conducted in *GraphPad Prism* and graphs were generated in *GraphPad Prism*.

Supplemental Information

Table S1: A list of all plasmids generated in this study. Details for all plasmids, including Addgene catalog #, subcellular localization, fluorophore, antibiotic resistance, and in which figure each plasmid was used.

Video S1: Mitochondrial axonal transport in *PRKN*$^{+/+}$ and *PRKN*$^{-/-}$ human iPSC derived neurons Representative videos of COX8A-Emerald labeled mitochondria moving within neuronal axons over the course of 1 hour. Images were taken every 10 seconds and sped up 70x. Scale bar = 25 µm. Related to Figure 4.

References

1. Willis, A.W., Roberts, E., Beck, J.C., Fiske, B., Ross, W., Savica, R., Van Den Eeden, S.K., Tanner, C.M., Marras, C., and Parkinson's Foundation, P.G. (2022). Incidence of Parkinson disease in North America. NPJ Parkinsons Dis *8*, 170. 10.1038/s41531-022-00410-y.
2. Vazquez-Velez, G.E., and Zoghbi, H.Y. (2021). Parkinson's Disease Genetics and Pathophysiology. Annu Rev Neurosci *44*, 87-108. 10.1146/annurev-neuro-100720-034518.
3. Schneider, S.A., and Obeso, J.A. (2015). Clinical and pathological features of Parkinson's disease. Curr Top Behav Neurosci *22*, 205-220. 10.1007/7854_2014_317.
4. Varadi, C. (2020). Clinical Features of Parkinson's Disease: The Evolution of Critical Symptoms. Biology (Basel) *9*. 10.3390/biology9050103.
5. Jankovic, J. (2008). Parkinson's disease: clinical features and diagnosis. J Neurol Neurosurg Psychiatry *79*, 368-376. 10.1136/jnnp.2007.131045.
6. Naoi, M., and Maruyama, W. (1999). Cell death of dopamine neurons in aging and Parkinson's disease. Mech Ageing Dev *111*, 175-188. 10.1016/s0047-6374(99)00064-0.
7. Spillantini, M.G., Schmidt, M.L., Lee, V.M., Trojanowski, J.Q., Jakes, R., and Goedert, M. (1997). Alpha-synuclein in Lewy bodies. Nature *388*, 839-840. 10.1038/42166.
8. Ohama, E., and Ikuta, F. (1976). Parkinson's disease: distribution of Lewy bodies and monoamine neuron system. Acta Neuropathol *34*, 311-319. 10.1007/BF00696560.
9. Hartmann, A. (2004). Postmortem studies in Parkinson's disease. Dialogues Clin Neurosci *6*, 281-293. 10.31887/DCNS.2004.6.3/ahartmann.
10. Helmchen, F., Fee, M.S., Tank, D.W., and Denk, W. (2001). A miniature head-mounted two-photon microscope. high-resolution brain imaging in freely moving animals. Neuron *31*, 903-912. 10.1016/s0896-6273(01)00421-4.

11. Zong, W., Wu, R., Li, M., Hu, Y., Li, Y., Li, J., Rong, H., Wu, H., Xu, Y., Lu, Y., et al. (2017). Fast high-resolution miniature two-photon microscopy for brain imaging in freely behaving mice. Nat Methods *14*, 713-719. 10.1038/nmeth.4305.
12. Chen, K., Tian, Z., and Kong, L. (2022). Advances of optical miniscopes for in vivo imaging of neural activity in freely moving animals. Front Neurosci *16*, 994079. 10.3389/fnins.2022.994079.
13. Potashkin, J.A., Blume, S.R., and Runkle, N.K. (2010). Limitations of animal models of Parkinson's disease. Parkinsons Dis *2011*, 658083. 10.4061/2011/658083.
14. Chia, S.J., Tan, E.K., and Chao, Y.X. (2020). Historical Perspective: Models of Parkinson's Disease. Int J Mol Sci *21*. 10.3390/ijms21072464.
15. Ahfeldt, T., Ordureau, A., Bell, C., Sarrafha, L., Sun, C., Piccinotti, S., Grass, T., Parfitt, G.M., Paulo, J.A., Yanagawa, F., et al. (2020). Pathogenic Pathways in Early-Onset Autosomal Recessive Parkinson's Disease Discovered Using Isogenic Human Dopaminergic Neurons. Stem Cell Reports *14*, 75-90. 10.1016/j.stemcr.2019.12.005.
16. Raja, W.K., Neves, E., Burke, C., Jiang, X., Xu, P., Rhodes, K.J., Khurana, V., Scannevin, R.H., and Chung, C.Y. (2022). Patient-derived three-dimensional cortical neurospheres to model Parkinson's disease. PLoS One *17*, e0277532. 10.1371/journal.pone.0277532.
17. Chlebanowska, P., Tejchman, A., Sulkowski, M., Skrzypek, K., and Majka, M. (2020). Use of 3D Organoids as a Model to Study Idiopathic Form of Parkinson's Disease. Int J Mol Sci *21*. 10.3390/ijms21030694.
18. Kim, H., Park, H.J., Choi, H., Chang, Y., Park, H., Shin, J., Kim, J., Lengner, C.J., Lee, Y.K., and Kim, J. (2019). Modeling G2019S-LRRK2 Sporadic Parkinson's Disease in 3D Midbrain Organoids. Stem Cell Reports *12*, 518-531. 10.1016/j.stemcr.2019.01.020.
19. Shimomura, O., Johnson, F.H., and Saiga, Y. (1962). Extraction, purification and properties of aequorin, a bioluminescent protein from the luminous hydromedusan, Aequorea. J Cell Comp Physiol *59*, 223-239. 10.1002/jcp.1030590302.
20. Wang, M., Da, Y., and Tian, Y. (2023). Fluorescent proteins and genetically encoded biosensors. Chem Soc Rev *52*, 1189-1214. 10.1039/d2cs00419d.
21. Ovechkina, V.S., Zakian, S.M., Medvedev, S.P., and Valetdinova, K.R. (2021). Genetically Encoded Fluorescent Biosensors for Biomedical Applications. Biomedicines *9*. 10.3390/biomedicines9111528.
22. Terskikh, A., Fradkov, A., Ermakova, G., Zaraisky, A., Tan, P., Kajava, A.V., Zhao, X., Lukyanov, S., Matz, M., Kim, S., et al. (2000). "Fluorescent timer": protein that changes color with time. Science *290*, 1585-1588. 10.1126/science.290.5496.1585.
23. Nakai, J., Ohkura, M., and Imoto, K. (2001). A high signal-to-noise Ca(2+) probe composed of a single green fluorescent protein. Nat Biotechnol *19*, 137-141. 10.1038/84397.
24. Burgstaller, S., Bischof, H., Gensch, T., Stryeck, S., Gottschalk, B., Ramadani-Muja, J., Eroglu, E., Rost, R., Balfanz, S., Baumann, A., et al. (2019). pH-Lemon, a Fluorescent Protein-Based pH Reporter for Acidic Compartments. ACS Sens *4*, 883-891. 10.1021/acssensors.8b01599.
25. Gutscher, M., Pauleau, A.L., Marty, L., Brach, T., Wabnitz, G.H., Samstag, Y., Meyer, A.J., and Dick, T.P. (2008). Real-time imaging of the intracellular glutathione redox potential. Nat Methods *5*, 553-559. 10.1038/nmeth.1212.
26. Nalls, M.A., Blauwendraat, C., Vallerga, C.L., Heilbron, K., Bandres-Ciga, S., Chang, D., Tan, M., Kia, D.A., Noyce, A.J., Xue, A., et al. (2019). Identification of novel risk loci, causal insights, and heritable risk for Parkinson's disease: a meta-analysis of genome-wide association studies. Lancet Neurol *18*, 1091-1102. 10.1016/S1474-4422(19)30320-5.
27. Karimi-Moghadam, A., Charsouei, S., Bell, B., and Jabalameli, M.R. (2018). Parkinson Disease from Mendelian Forms to Genetic Susceptibility: New Molecular Insights into the

Neurodegeneration Process. Cell Mol Neurobiol *38*, 1153-1178. 10.1007/s10571-018-0587-4.

28. Jia, F., Fellner, A., and Kumar, K.R. (2022). Monogenic Parkinson's Disease: Genotype, Phenotype, Pathophysiology, and Genetic Testing. Genes (Basel) *13*. 10.3390/genes13030471.
29. Guadagnolo, D., Piane, M., Torrisi, M.R., Pizzuti, A., and Petrucci, S. (2021). Genotype-Phenotype Correlations in Monogenic Parkinson Disease: A Review on Clinical and Molecular Findings. Front Neurol *12*, 648588. 10.3389/fneur.2021.648588.
30. Lesage, S., Lunati, A., Houot, M., Romdhan, S.B., Clot, F., Tesson, C., Mangone, G., Toullec, B.L., Courtin, T., Larcher, K., et al. (2020). Characterization of Recessive Parkinson Disease in a Large Multicenter Study. Ann Neurol *88*, 843-850. 10.1002/ana.25787.
31. Pickrell, A.M., and Youle, R.J. (2015). The roles of PINK1, parkin, and mitochondrial fidelity in Parkinson's disease. Neuron *85*, 257-273. 10.1016/j.neuron.2014.12.007.
32. Tanaka, K. (2020). The PINK1-Parkin axis: An Overview. Neurosci Res *159*, 9-15. 10.1016/j.neures.2020.01.006.
33. Kamienieva, I., Duszynski, J., and Szczepanowska, J. (2021). Multitasking guardian of mitochondrial quality: Parkin function and Parkinson's disease. Transl Neurodegener *10*, 5. 10.1186/s40035-020-00229-8.
34. Lois, C., Hong, E.J., Pease, S., Brown, E.J., and Baltimore, D. (2002). Germline transmission and tissue-specific expression of transgenes delivered by lentiviral vectors. Science *295*, 868-872. 10.1126/science.1067081.
35. Schorpp, M., Jäger, R., Schellander, K., Schenkel, J., Wagner, E.F., Weiher, H., and Angel, P. (1996/05/01). The Human Ubiquitin C Promoter Directs High Ubiquitous Expression of Transgenes in Mice. Nucleic Acids Research *24*. 10.1093/nar/24.9.1787.
36. Zufferey, R., Donello, J.E., Trono, D., and Hope, T.J. (1999/04). Woodchuck Hepatitis Virus Posttranscriptional Regulatory Element Enhances Expression of Transgenes Delivered by Retroviral Vectors. Journal of Virology *73*. 10.1128/jvi.73.4.2886-2892.1999.
37. Higashimoto, T., Urbinati, F., Perumbeti, A., Jiang, G., Zarzuela, A., Chang, L.J., Kohn, D.B., and Malik, P. (2007). The woodchuck hepatitis virus post-transcriptional regulatory element reduces readthrough transcription from retroviral vectors. Gene Therapy *14*, 1298-1304. 10.1038/sj.gt.3302979.
38. Mosammaparast, N., Jackson, K.R., Guo, Y., Brame, C.J., Shabanowitz, J., Hunt, D.F., and Pemberton, L.F. (2001). Nuclear import of histone H2A and H2B is mediated by a network of karyopherins. J Cell Biol *153*, 251-262. 10.1083/jcb.153.2.251.
39. Marino-Ramirez, L., Kann, M.G., Shoemaker, B.A., and Landsman, D. (2005). Histone structure and nucleosome stability. Expert Rev Proteomics *2*, 719-729. 10.1586/14789450.2.5.719.
40. Smith, P.J., Wiltshire, M., and Errington, R.J. (2004). DRAQ5 labeling of nuclear DNA in live and fixed cells. Curr Protoc Cytom *Chapter 7*, Unit 7 25. 10.1002/0471142956.cy0725s28.
41. Zhitomirsky, B., Farber, H., and Assaraf, Y.G. (2018). LysoTracker and MitoTracker Red are transport substrates of P-glycoprotein: implications for anticancer drug design evading multidrug resistance. J Cell Mol Med *22*, 2131-2141. 10.1111/jcmm.13485.
42. Chazotte, B. (2011). Labeling lysosomes in live cells with LysoTracker. Cold Spring Harb Protoc *2011*, pdb prot5571. 10.1101/pdb.prot5571.
43. Dang, Q., Zhou, H., Qian, J., Yang, L., Huang, J., Zhang, Y., and Shi, W. (2018). LAMP1 Overexpression Predicts for Poor Prognosis in Diffuse Large B-cell Lymphoma. Clin Lymphoma Myeloma Leuk *18*, 749-754. 10.1016/j.clml.2018.07.288.

1001 44. Wang, Q.Q., Yao, J., Jin, Q., Wang, X.D., Zhu, H.J., Huang, F., Wang, W., Qiang, J.F., and
1002 Ni, Q.C. (2017). LAMP1 expression is associated with poor prognosis in breast cancer.
1003 Oncol Lett *14*, 4729-4735. 10.3892/ol.2017.6757.
1004 45. Xu, Y., Cao, X., Zhang, S., Zhang, Y., and Shen, Z. (2017). High expression of LAMP1 as
1005 a prognostic marker in patients with epithelial ovarian cancer. Int J Clin Exp Pathol *10*,
1006 9104-9111.
1007 46. Ranjbar, M.A., and Jamshidi, M. (2022). Overexpression of Lysosome-Associated
1008 Membrane Protein 1 in Oral Squamous Cell Carcinoma and its Correlation with Tumor
1009 Differentiation and Metastasis. Iran J Otorhinolaryngol *34*, 3-8.
1010 10.22038/IJORL.2021.51683.2772.
1011 47. Zong, S., Wu, M., Gu, J., Liu, T., Guo, R., and Yang, M. (2018). Structure of the intact 14-
1012 subunit human cytochrome c oxidase. Cell Res *28*, 1026-1034. 10.1038/s41422-018-
1013 0071-1.
1014 48. Cunatova, K., Reguera, D.P., Houstek, J., Mracek, T., and Pecina, P. (2020). Role of
1015 cytochrome c oxidase nuclear-encoded subunits in health and disease. Physiol Res *69*,
1016 947-965. 10.33549/physiolres.934446.
1017 49. Partikian, A., Olveczky, B., Swaminathan, R., Li, Y., and Verkman, A.S. (1998). Rapid
1018 diffusion of green fluorescent protein in the mitochondrial matrix. J Cell Biol *140*, 821-829.
1019 10.1083/jcb.140.4.821.
1020 50. Hoogewijs, K., James, A.M., Smith, R.A., Gait, M.J., Murphy, M.P., and Lightowlers, R.N.
1021 (2016). Assessing the Delivery of Molecules to the Mitochondrial Matrix Using Click
1022 Chemistry. Chembiochem *17*, 1312-1316. 10.1002/cbic.201600188.
1023 51. Candas, D., Qin, L., Fan, M., and Li, J.J. (2016). Experimental Approaches to Study
1024 Mitochondrial Localization and Function of a Nuclear Cell Cycle Kinase, Cdk1. J Vis Exp,
1025 53417. 10.3791/53417.
1026 52. Chazotte, B. (2011). Labeling mitochondria with MitoTracker dyes. Cold Spring Harb
1027 Protoc *2011*, 990-992. 10.1101/pdb.prot5648.
1028 53. Durand, R.E., and Olive, P.L. (1982). Cytotoxicity, Mutagenicity and DNA damage by
1029 Hoechst 33342. J Histochem Cytochem *30*, 111-116. 10.1177/30.2.7061816.
1030 54. Wiezorek, C. (1984). Cell cycle dependence of Hoechst 33342 dye cytotoxicity on sorted
1031 living cells. Histochemistry *81*, 493-495. 10.1007/BF00489756.
1032 55. Solano, R.M., Casarejos, M.J., Menendez-Cuervo, J., Rodriguez-Navarro, J.A., Garcia de
1033 Yebenes, J., and Mena, M.A. (2008). Glial dysfunction in parkin null mice: effects of aging.
1034 J Neurosci *28*, 598-611. 10.1523/JNEUROSCI.4609-07.2008.
1035 56. Rouland, L., Duplan, E., Ramos Dos Santos, L., Bernardin, A., Katula, K.S., Manfioletti,
1036 G., Idbaih, A., Checler, F., and Alves da Costa, C. (2021). Therapeutic potential of parkin
1037 as a tumor suppressor via transcriptional control of cyclins in glioblastoma cell and animal
1038 models. Theranostics *11*, 10047-10063. 10.7150/thno.57549.
1039 57. Wahabi, K., Perwez, A., and Rizvi, M.A. (2018). Parkin in Parkinson's Disease and Cancer:
1040 a Double-Edged Sword. Mol Neurobiol *55*, 6788-6800. 10.1007/s12035-018-0879-1.
1041 58. Yeo, C.W., Ng, F.S., Chai, C., Tan, J.M., Koh, G.R., Chong, Y.K., Koh, L.W., Foong, C.S.,
1042 Sandanaraj, E., Holbrook, J.D., et al. (2012). Parkin pathway activation mitigates glioma
1043 cell proliferation and predicts patient survival. Cancer Res *72*, 2543-2553. 10.1158/0008-
1044 5472.CAN-11-3060.
1045 59. Tay, S.P., Yeo, C.W., Chai, C., Chua, P.J., Tan, H.M., Ang, A.X., Yip, D.L., Sung, J.X., Tan,
1046 P.H., Bay, B.H., et al. (2010). Parkin enhances the expression of cyclin-dependent kinase
1047 6 and negatively regulates the proliferation of breast cancer cells. J Biol Chem *285*, 29231-
1048 29238. 10.1074/jbc.M110.108241.
1049 60. Gong, Y., Zack, T.I., Morris, L.G., Lin, K., Hukkelhoven, E., Raheja, R., Tan, I.L., Turcan,
1050 S., Veeriah, S., Meng, S., et al. (2014). Pan-cancer genetic analysis identifies PARK2 as
1051 a master regulator of G1/S cyclins. Nat Genet *46*, 588-594. 10.1038/ng.2981.

1052 61. Veeriah, S., Morris, L., Solit, D., and Chan, T.A. (2010). The familial Parkinson disease
1053 gene PARK2 is a multisite tumor suppressor on chromosome 6q25.2-27 that regulates
1054 cyclin E. Cell Cycle *9*, 1451-1452. 10.4161/cc.9.8.11583.
1055 62. Veeriah, S., Taylor, B.S., Meng, S., Fang, F., Yilmaz, E., Vivanco, I., Janakiraman, M.,
1056 Schultz, N., Hanrahan, A.J., Pao, W., et al. (2010). Somatic mutations of the Parkinson's
1057 disease-associated gene PARK2 in glioblastoma and other human malignancies. Nat
1058 Genet *42*, 77-82. 10.1038/ng.491.
1059 63. Frade, J.M., and Ovejero-Benito, M.C. (2015). Neuronal cell cycle: the neuron itself and
1060 its circumstances. Cell Cycle *14*, 712-720. 10.1080/15384101.2015.1004937.
1061 64. Kruman, II, Wersto, R.P., Cardozo-Pelaez, F., Smilenov, L., Chan, S.L., Chrest, F.J.,
1062 Emokpae, R., Jr., Gorospe, M., and Mattson, M.P. (2004). Cell cycle activation linked to
1063 neuronal cell death initiated by DNA damage. Neuron *41*, 549-561. 10.1016/s0896-
1064 6273(04)00017-0.
1065 65. Gan-Or, Z., Dion, P.A., and Rouleau, G.A. (2015). Genetic perspective on the role of the
1066 autophagy-lysosome pathway in Parkinson disease. Autophagy *11*, 1443-1457.
1067 10.1080/15548627.2015.1067364.
1068 66. Navarro-Romero, A., Montpeyo, M., and Martinez-Vicente, M. (2020). The Emerging Role
1069 of the Lysosome in Parkinson's Disease. Cells *9*. 10.3390/cells9112399.
1070 67. Hopfner, F., Mueller, S.H., Szymczak, S., Junge, O., Tittmann, L., May, S., Lohmann, K.,
1071 Grallert, H., Lieb, W., Strauch, K., et al. (2020). Rare Variants in Specific Lysosomal Genes
1072 Are Associated With Parkinson's Disease. Mov Disord *35*, 1245-1248.
1073 10.1002/mds.28037.
1074 68. Dehay, B., Martinez-Vicente, M., Caldwell, G.A., Caldwell, K.A., Yue, Z., Cookson, M.R.,
1075 Klein, C., Vila, M., and Bezard, E. (2013). Lysosomal impairment in Parkinson's disease.
1076 Mov Disord *28*, 725-732. 10.1002/mds.25462.
1077 69. Klein, A.D., and Mazzulli, J.R. (2018). Is Parkinson's disease a lysosomal disorder? Brain
1078 *141*, 2255-2262. 10.1093/brain/awy147.
1079 70. Yoshimori, T., Yamamoto, A., Moriyama, Y., Futai, M., and Tashiro, Y. (1991). Bafilomycin
1080 A1, a specific inhibitor of vacuolar-type H(+)-ATPase, inhibits acidification and protein
1081 degradation in lysosomes of cultured cells. J Biol Chem *266*, 17707-17712.
1082 71. Mauvezin, C., and Neufeld, T.P. (2015). Bafilomycin A1 disrupts autophagic flux by
1083 inhibiting both V-ATPase-dependent acidification and Ca-P60A/SERCA-dependent
1084 autophagosome-lysosome fusion. Autophagy *11*, 1437-1438.
1085 10.1080/15548627.2015.1066957.
1086 72. Carpenter, A.E., Jones, T.R., Lamprecht, M.R., Clarke, C., Kang, I.H., Friman, O., Guertin,
1087 D.A., Chang, J.H., Lindquist, R.A., Moffat, J., et al. (2006). CellProfiler: image analysis
1088 software for identifying and quantifying cell phenotypes. Genome Biol *7*, R100.
1089 10.1186/gb-2006-7-10-r100.
1090 73. Johnson, D.E., Ostrowski, P., Jaumouille, V., and Grinstein, S. (2016). The position of
1091 lysosomes within the cell determines their luminal pH. J Cell Biol *212*, 677-692.
1092 10.1083/jcb.201507112.
1093 74. Heuser, J. (1989). Changes in lysosome shape and distribution correlated with changes
1094 in cytoplasmic pH. J Cell Biol *108*, 855-864. 10.1083/jcb.108.3.855.
1095 75. Parton, R.G., Dotti, C.G., Bacallao, R., Kurtz, I., Simons, K., and Prydz, K. (1991). pH-
1096 induced microtubule-dependent redistribution of late endosomes in neuronal and epithelial
1097 cells. J Cell Biol *113*, 261-274. 10.1083/jcb.113.2.261.
1098 76. Pu, J., Guardia, C.M., Keren-Kaplan, T., and Bonifacino, J.S. (2016). Mechanisms and
1099 functions of lysosome positioning. J Cell Sci *129*, 4329-4339. 10.1242/jcs.196287.
1100 77. Song, P., Trajkovic, K., Tsunemi, T., and Krainc, D. (2016). Parkin Modulates Endosomal
1101 Organization and Function of the Endo-Lysosomal Pathway. J Neurosci *36*, 2425-2437.
1102 10.1523/JNEUROSCI.2569-15.2016.

78. Okarmus, J., Bogetofte, H., Schmidt, S.I., Ryding, M., Garcia-Lopez, S., Ryan, B.J., Martinez-Serrano, A., Hyttel, P., and Meyer, M. (2020). Lysosomal perturbations in human dopaminergic neurons derived from induced pluripotent stem cells with PARK2 mutation. Sci Rep *10*, 10278. 10.1038/s41598-020-67091-6.
79. Twig, G., Elorza, A., Molina, A.J., Mohamed, H., Wikstrom, J.D., Walzer, G., Stiles, L., Haigh, S.E., Katz, S., Las, G., et al. (2008). Fission and selective fusion govern mitochondrial segregation and elimination by autophagy. EMBO J *27*, 433-446. 10.1038/sj.emboj.7601963.
80. Chen, H., Chomyn, A., and Chan, D.C. (2005). Disruption of fusion results in mitochondrial heterogeneity and dysfunction. J Biol Chem *280*, 26185-26192. 10.1074/jbc.M503062200.
81. Sarrafha, L., Parfitt, G.M., Reyes, R., Goldman, C., Coccia, E., Kareva, T., and Ahfeldt, T. (2021). High-throughput generation of midbrain dopaminergic neuron organoids from reporter human pluripotent stem cells. STAR Protoc *2*, 100463. 10.1016/j.xpro.2021.100463.
82. Wang, X., Winter, D., Ashrafi, G., Schlehe, J., Wong, Y.L., Selkoe, D., Rice, S., Steen, J., LaVoie, M.J., and Schwarz, T.L. (2011). PINK1 and Parkin target Miro for phosphorylation and degradation to arrest mitochondrial motility. Cell *147*, 893-906. 10.1016/j.cell.2011.10.018.
83. Hernandez, G., Thornton, C., Stotland, A., Lui, D., Sin, J., Ramil, J., Magee, N., Andres, A., Quarato, G., Carreira, R.S., et al. (2013). MitoTimer: a novel tool for monitoring mitochondrial turnover. Autophagy *9*, 1852-1861. 10.4161/auto.26501.
84. Laker, R.C., Xu, P., Ryall, K.A., Sujkowski, A., Kenwood, B.M., Chain, K.H., Zhang, M., Royal, M.A., Hoehn, K.L., Driscoll, M., et al. (2014). A novel MitoTimer reporter gene for mitochondrial content, structure, stress, and damage in vivo. J Biol Chem *289*, 12005-12015. 10.1074/jbc.M113.530527.
85. Stauch, K.L., Totusek, S., Trease, A.J., Estrella, L.D., Emanuel, K., Fangmeier, A., and Fox, H.S. (2023). Longitudinal in vivo metabolic labeling reveals tissue-specific mitochondrial proteome turnover rates and proteins selectively altered by parkin deficiency. Sci Rep *13*, 11414. 10.1038/s41598-023-38484-0.
86. Hanson, G.T., Aggeler, R., Oglesbee, D., Cannon, M., Capaldi, R.A., Tsien, R.Y., and Remington, S.J. (2004). Investigating mitochondrial redox potential with redox-sensitive green fluorescent protein indicators. J Biol Chem *279*, 13044-13053. 10.1074/jbc.M312846200.
87. Yokomakura, A., Hong, J., Ohuchi, K., Oh, S.E., Lee, J.Y., Mano, N., Takahashi, T., Hwang, G.W., and Naganuma, A. (2012). Increased production of reactive oxygen species by the vacuolar-type (H(+))-ATPase inhibitors bafilomycin A1 and concanamycin A in RAW 264 cells. J Toxicol Sci *37*, 1045-1048. 10.2131/jts.37.1045.
88. Palacino, J.J., Sagi, D., Goldberg, M.S., Krauss, S., Motz, C., Wacker, M., Klose, J., and Shen, J. (2004). Mitochondrial dysfunction and oxidative damage in parkin-deficient mice. J Biol Chem *279*, 18614-18622. 10.1074/jbc.M401135200.
89. Cornejo-Olivas, M.R., Torres, L., Mata, I.F., Mazzetti, P., Rivas, D., Cosentino, C., Inca-Martinez, M., Cuba, J.M., Zabetian, C.P., and Leverenz, J.B. (2015). A Peruvian family with a novel PARK2 mutation: Clinical and pathological characteristics. Parkinsonism Relat Disord *21*, 444-448. 10.1016/j.parkreldis.2015.01.005.
90. Orimo, S., Amino, T., Yokochi, M., Kojo, T., Uchihara, T., Takahashi, A., Wakabayashi, K., Takahashi, H., Hattori, N., and Mizuno, Y. (2005). Preserved cardiac sympathetic nerve accounts for normal cardiac uptake of MIBG in PARK2. Mov Disord *20*, 1350-1353. 10.1002/mds.20594.
91. Gouider-Khouja, N., Larnaout, A., Amouri, R., Sfar, S., Belal, S., Ben Hamida, C., Ben Hamida, M., Hattori, N., Mizuno, Y., and Hentati, F. (2003). Autosomal recessive

parkinsonism linked to parkin gene in a Tunisian family. Clinical, genetic and pathological study. Parkinsonism Relat Disord *9*, 247-251. 10.1016/s1353-8020(03)00016-6.

92. Hayashi, S., Wakabayashi, K., Ishikawa, A., Nagai, H., Saito, M., Maruyama, M., Takahashi, T., Ozawa, T., Tsuji, S., and Takahashi, H. (2000). An autopsy case of autosomal-recessive juvenile parkinsonism with a homozygous exon 4 deletion in the parkin gene. Mov Disord *15*, 884-888. 10.1002/1531-8257(200009)15:5<884::aid-mds1019>3.0.co;2-8.
93. Schmidt, S., Linnartz, B., Mendritzki, S., Sczepan, T., Lubbert, M., Stichel, C.C., and Lubbert, H. (2011). Genetic mouse models for Parkinson's disease display severe pathology in glial cell mitochondria. Hum Mol Genet *20*, 1197-1211. 10.1093/hmg/ddq564.
94. Gerasimova, T., Stepanenko, E., Novosadova, L., Arsenyeva, E., Shimchenko, D., Tarantul, V., Grivennikov, I., Nenasheva, V., and Novosadova, E. (2023). Glial Cultures Differentiated from iPSCs of Patients with PARK2-Associated Parkinson's Disease Demonstrate a Pro-Inflammatory Shift and Reduced Response to TNFalpha Stimulation. Int J Mol Sci *24*. 10.3390/ijms24032000.
95. Hastie, E., Cataldi, M., Marriott, I., and Grdzelishvili, V.Z. (2013). Understanding and altering cell tropism of vesicular stomatitis virus. Virus Res *176*, 16-32. 10.1016/j.virusres.2013.06.003.
96. Sweeney, N.P., and Vink, C.A. (2021). The impact of lentiviral vector genome size and producer cell genomic to gag-pol mRNA ratios on packaging efficiency and titre. Mol Ther Methods Clin Dev *21*, 574-584. 10.1016/j.omtm.2021.04.007.
97. Desfarges, S., and Ciuffi, A. (2010). Retroviral integration site selection. Viruses *2*, 111-130. 10.3390/v2010111.
98. Bonam, S.R., Wang, F., and Muller, S. (2019). Lysosomes as a therapeutic target. Nat Rev Drug Discov *18*, 923-948. 10.1038/s41573-019-0036-1.
99. Zhang, Z., Yue, P., Lu, T., Wang, Y., Wei, Y., and Wei, X. (2021). Role of lysosomes in physiological activities, diseases, and therapy. J Hematol Oncol *14*, 79. 10.1186/s13045-021-01087-1.
100. Javadov, S., Kozlov, A.V., and Camara, A.K.S. (2020). Mitochondria in Health and Diseases. Cells *9*. 10.3390/cells9051177.
101. Chen, W., Zhao, H., and Li, Y. (2023). Mitochondrial dynamics in health and disease: mechanisms and potential targets. Signal Transduct Target Ther *8*, 333. 10.1038/s41392-023-01547-9.
102. Dull, T., Zufferey, R., Kelly, M., Mandel, R.J., Nguyen, M., Trono, D., and Naldini, L. (1998). A third-generation lentivirus vector with a conditional packaging system. J Virol *72*, 8463-8471. 10.1128/JVI.72.11.8463-8471.1998.
103. Morrone Parfitt, G., Coccia, E., Goldman, C., Whitney, K., Reyes, R., Sarrafha, L., Nam, K.H., Sohail, S., Jones, D.R., Crary, J.F., et al. (2024). Disruption of lysosomal proteolysis in astrocytes facilitates midbrain organoid proteostasis failure in an early-onset Parkinson's disease model. Nat Commun *15*, 447. 10.1038/s41467-024-44732-2.
104. Chaudhry, A., Shi, R., and Luciani, D.S. (2020). A pipeline for multidimensional confocal analysis of mitochondrial morphology, function, and dynamics in pancreatic beta-cells. Am J Physiol Endocrinol Metab *318*, E87-E101. 10.1152/ajpendo.00457.2019.
105. Mangeol, P., Prevo, B., and Peterman, E.J. (2016). KymographClear and KymographDirect: two tools for the automated quantitative analysis of molecular and cellular dynamics using kymographs. Mol Biol Cell *27*, 1948-1957. 10.1091/mbc.E15-06-0404.
106. Stirling, D.R., Swain-Bowden, M.J., Lucas, A.M., Carpenter, A.E., Cimini, B.A., and Goodman, A. (2021). CellProfiler 4: improvements in speed, utility and usability. BMC Bioinformatics *22*, 433. 10.1186/s12859-021-04344-9.

107. Schindelin, J., Arganda-Carreras, I., Frise, E., Kaynig, V., Longair, M., Pietzsch, T., Preibisch, S., Rueden, C., Saalfeld, S., Schmid, B., et al. (2012). Fiji: an open-source platform for biological-image analysis. Nat Methods *9*, 676-682. 10.1038/nmeth.2019.

Figure 1

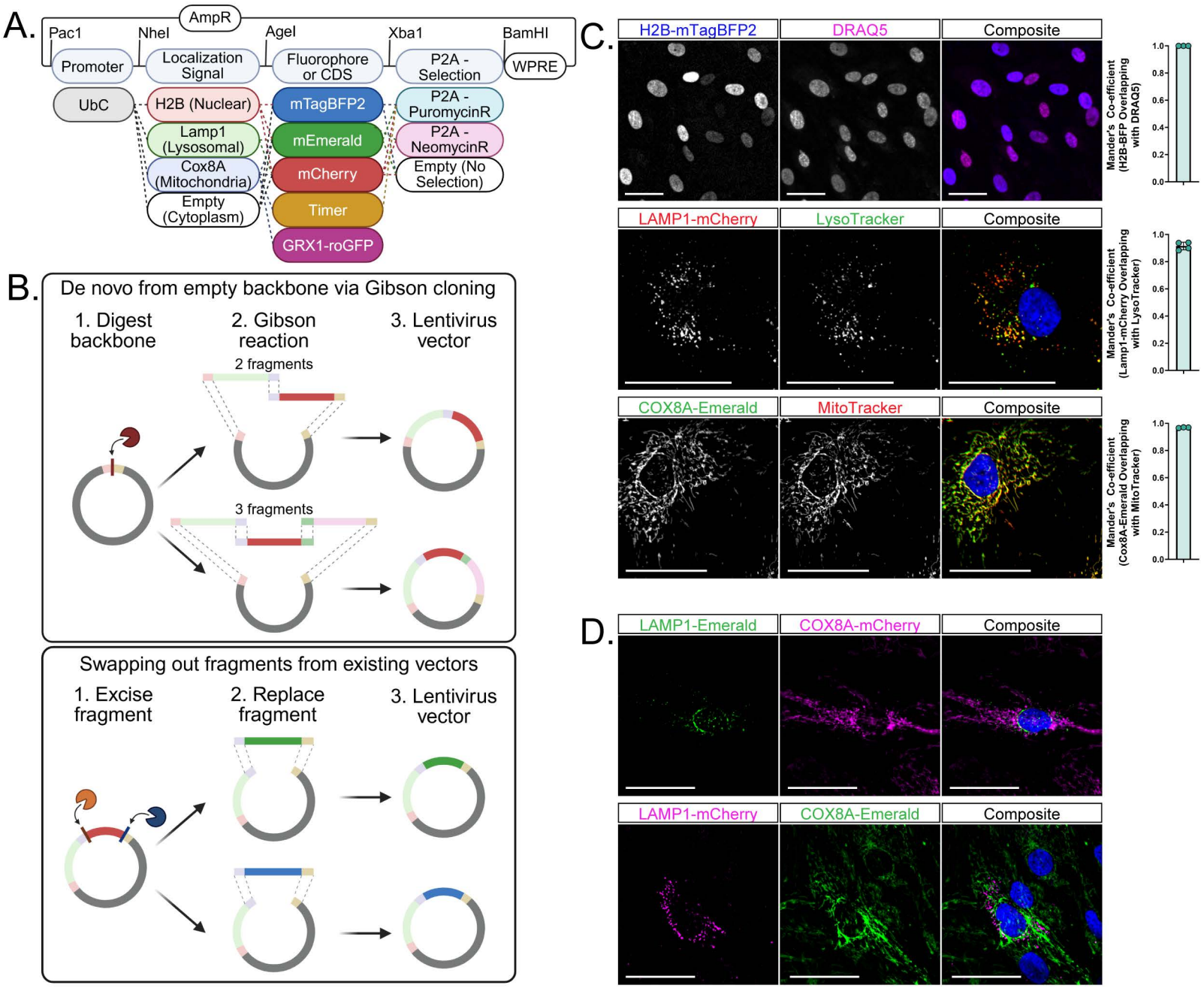
A.
AmpR
Pac1
NheI
AgeI
Xba1
BamHI
Promoter
Localization Signal
Fluorophore or CDS
P2A - Selection
WPRE
UbC
H2B (Nuclear)
Lamp1 (Lysosomal)
Cox8A (Mitochondria)
Empty (Cytoplasm)
mTagBFP2
mEmerald
mCherry
Timer
GRX1-roGFP
P2A - PuromycinR
P2A - NeomycinR
Empty (No Selection)
B.
De novo from empty backbone via Gibson cloning
1. Digest backbone
2. Gibson reaction
3. Lentivirus vector
2 fragments
3 fragments
Swapping out fragments from existing vectors
1. Excise fragment
2. Replace fragment
3. Lentivirus vector
C.
H2B-mTagBFP2
DRAQ5
Composite
Mander's Co-efficient (H2B-BFP Overlapping with DRAQ5)
LAMP1-mCherry
LysoTracker
Composite
Mander's Co-efficient (Lamp1-mCherry Overlapping with LysoTracker)
COX8A-Emerald
MitoTracker
Composite
Mander's Co-efficient (Cox8A-Emerald Overlapping with MitoTracker)
D.
LAMP1-Emerald
COX8A-mCherry
Composite
LAMP1-mCherry
COX8A-Emerald
Composite

Figure 2

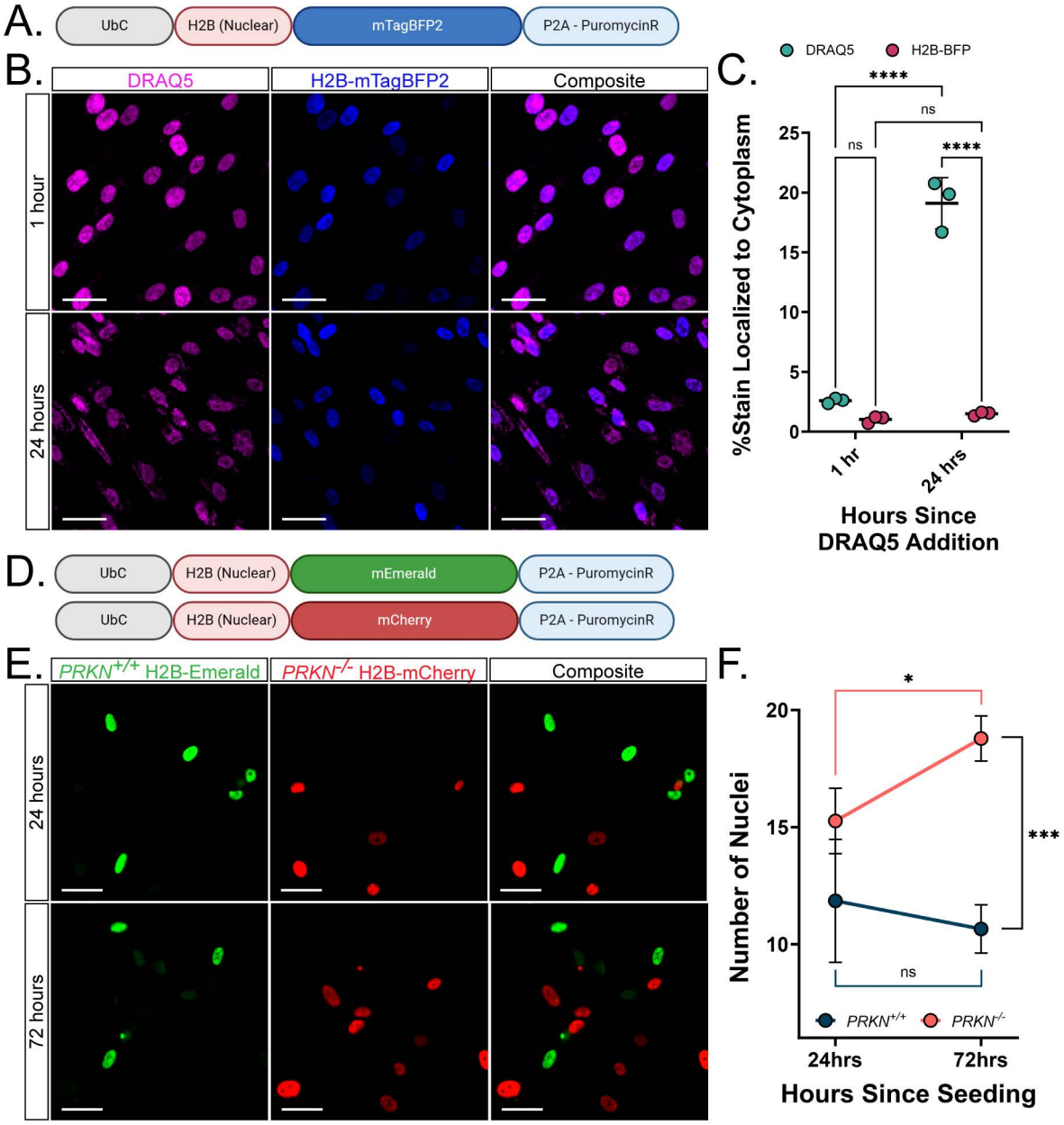
A.
UbC
H2B (Nuclear)
mTagBFP2
P2A - PuromycinR
B.
DRAQ5
H2B-mTagBFP2
Composite
1 hour
24 hours
C.
DRAQ5
H2B-BFP
****
ns
ns
****
%Stain Localized to Cytoplasm
25
20
15
10
5
0
1 hr
24 hrs
Hours Since
DRAQ5 Addition
D.
UbC
H2B (Nuclear)
mEmerald
P2A - PuromycinR
UbC
H2B (Nuclear)
mCherry
P2A - PuromycinR
E.
PRKN+/+ H2B-Emerald
PRKN-/- H2B-mCherry
Composite
24 hours
72 hours
F.
*
***
ns
Number of Nuclei
20
15
10
PRKN+/+
PRKN-/-
24hrs
72hrs
Hours Since Seeding

Figure 3

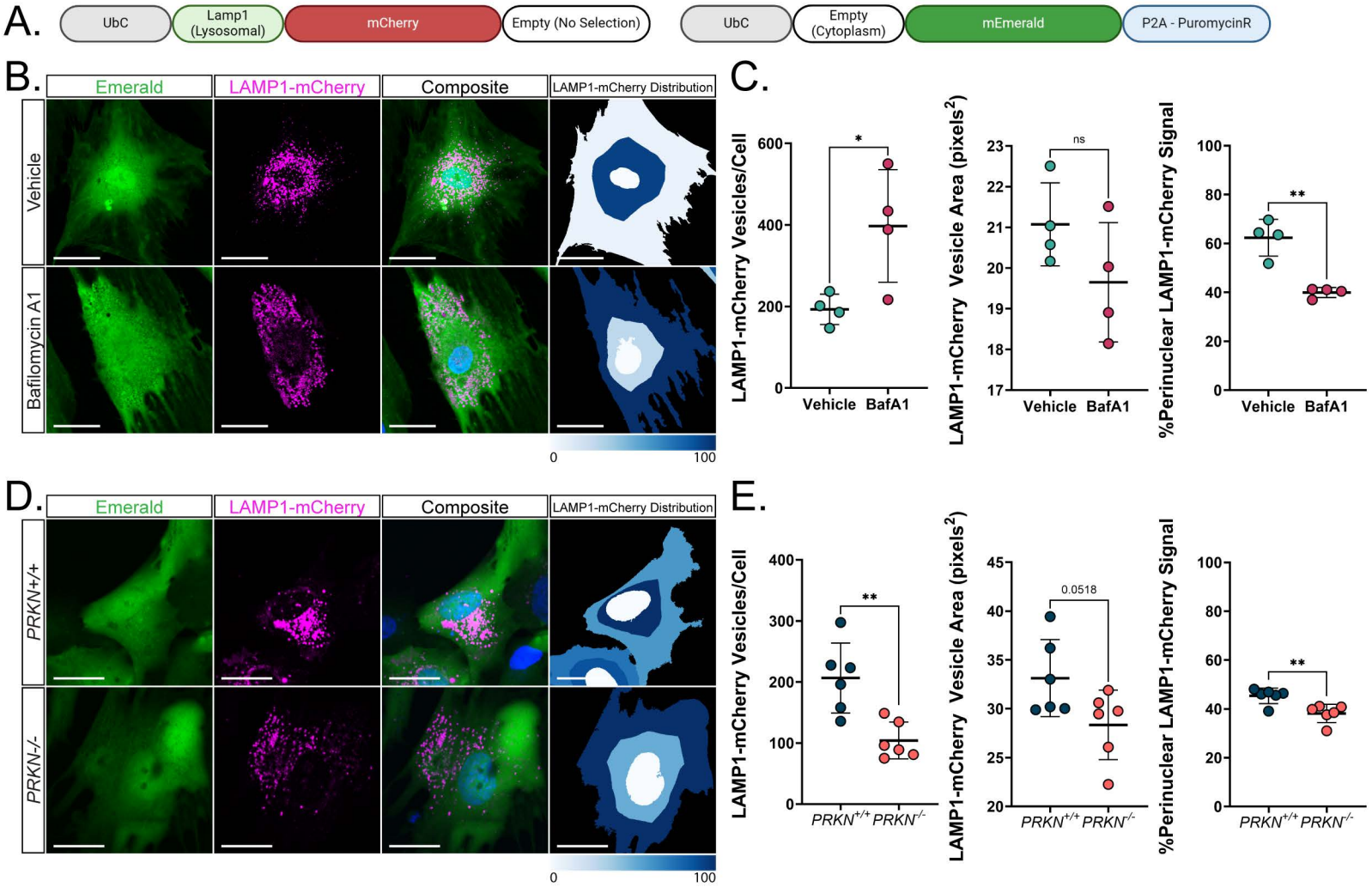
A.
UbC
Lamp1 (Lysosomal)
mCherry
Empty (No Selection)
UbC
Empty (Cytoplasm)
mEmerald
P2A - PuromycinR
B.
Emerald
LAMP1-mCherry
Composite
LAMP1-mCherry Distribution
Vehicle
Bafilomycin A1
0
100
C.
LAMP1-mCherry Vesicles/Cell
*
Vehicle
BafA1
LAMP1-mCherry Vesicle Area (pixels²)
ns
%Perinuclear LAMP1-mCherry Signal
**
D.
PRKN+/+
PRKN-/-
E.
**
0.0518
**
PRKN+/+
PRKN-/-

Figure 4

A.

B.

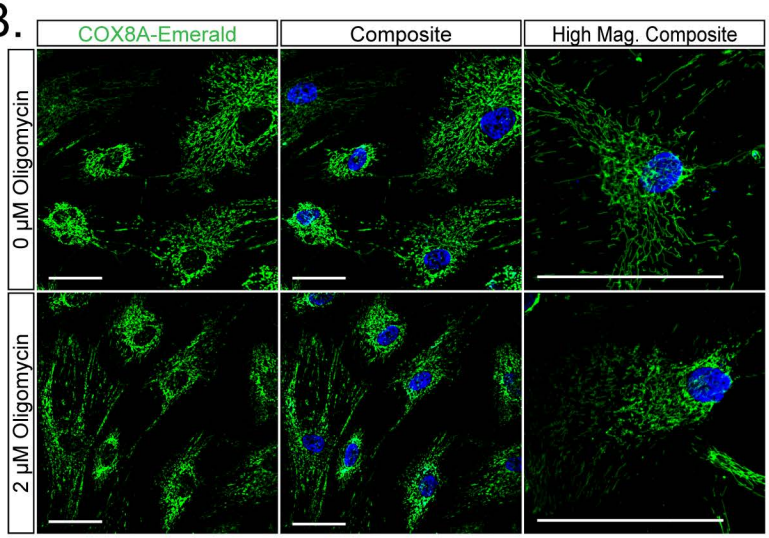

C.

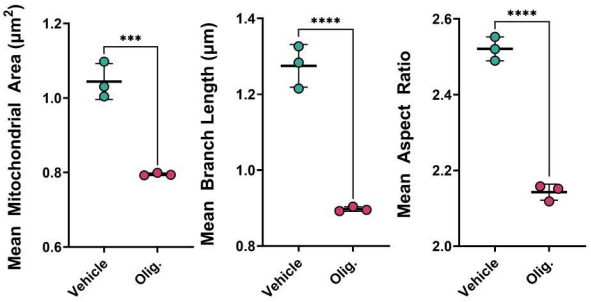

D.

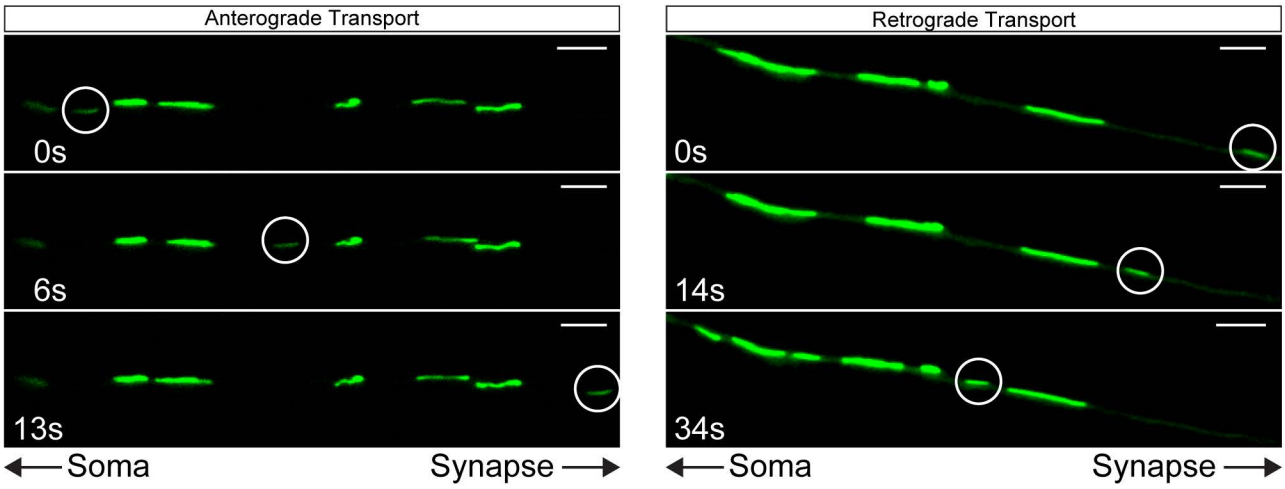

E.

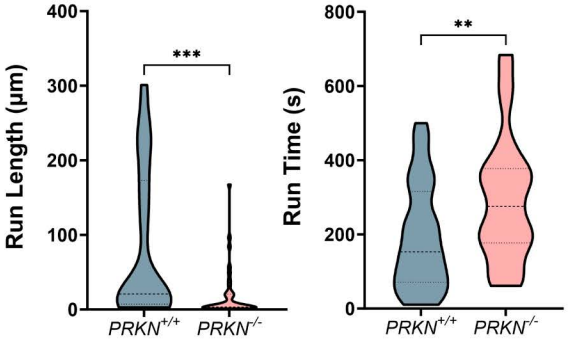

F.

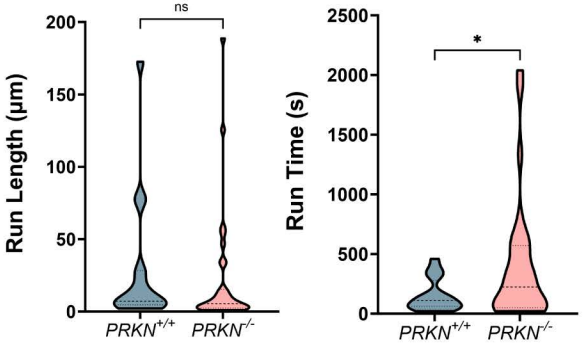

Figure 5

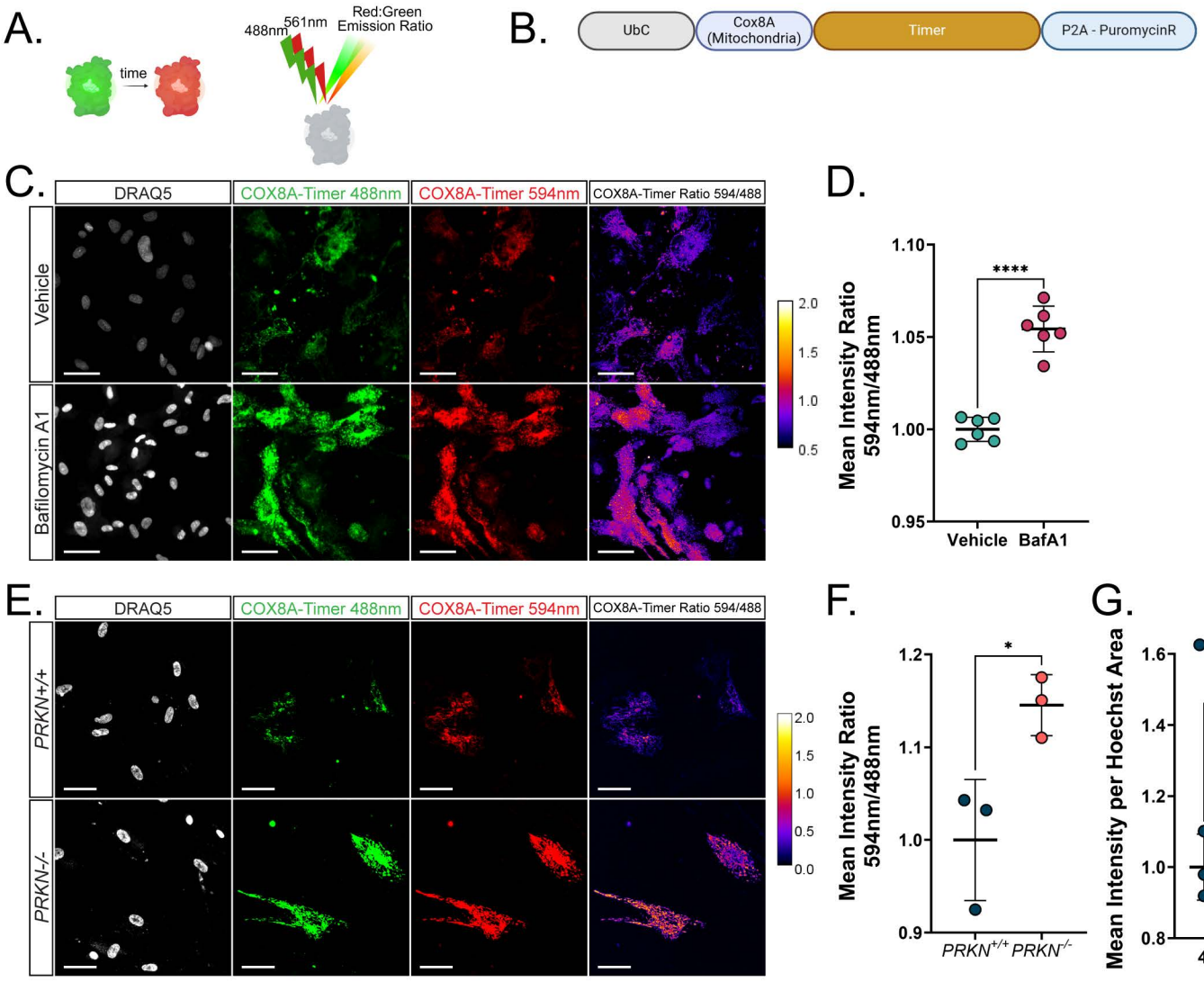
A.
time
488nm
561nm
Red:Green Emission Ratio
B.
UbC
Cox8A (Mitochondria)
Timer
P2A - PuromycinR
C.
DRAQ5
COX8A-Timer 488nm
COX8A-Timer 594nm
COX8A-Timer Ratio 594/488
Vehicle
Bafilomycin A1
2.0
1.5
1.0
0.5
D.
Mean Intensity Ratio 594nm/488nm
****
Vehicle
BafA1
E.
DRAQ5
COX8A-Timer 488nm
COX8A-Timer 594nm
COX8A-Timer Ratio 594/488
PRKN+/+
PRKN-/-
2.0
1.5
1.0
0.5
0.0
F.
Mean Intensity Ratio 594nm/488nm
*
PRKN+/+
PRKN-/-
G.
Mean Intensity per Hoechst Area
PRKN+/+
PRKN-/-
ns
*
488nm
594nm

Figure 6

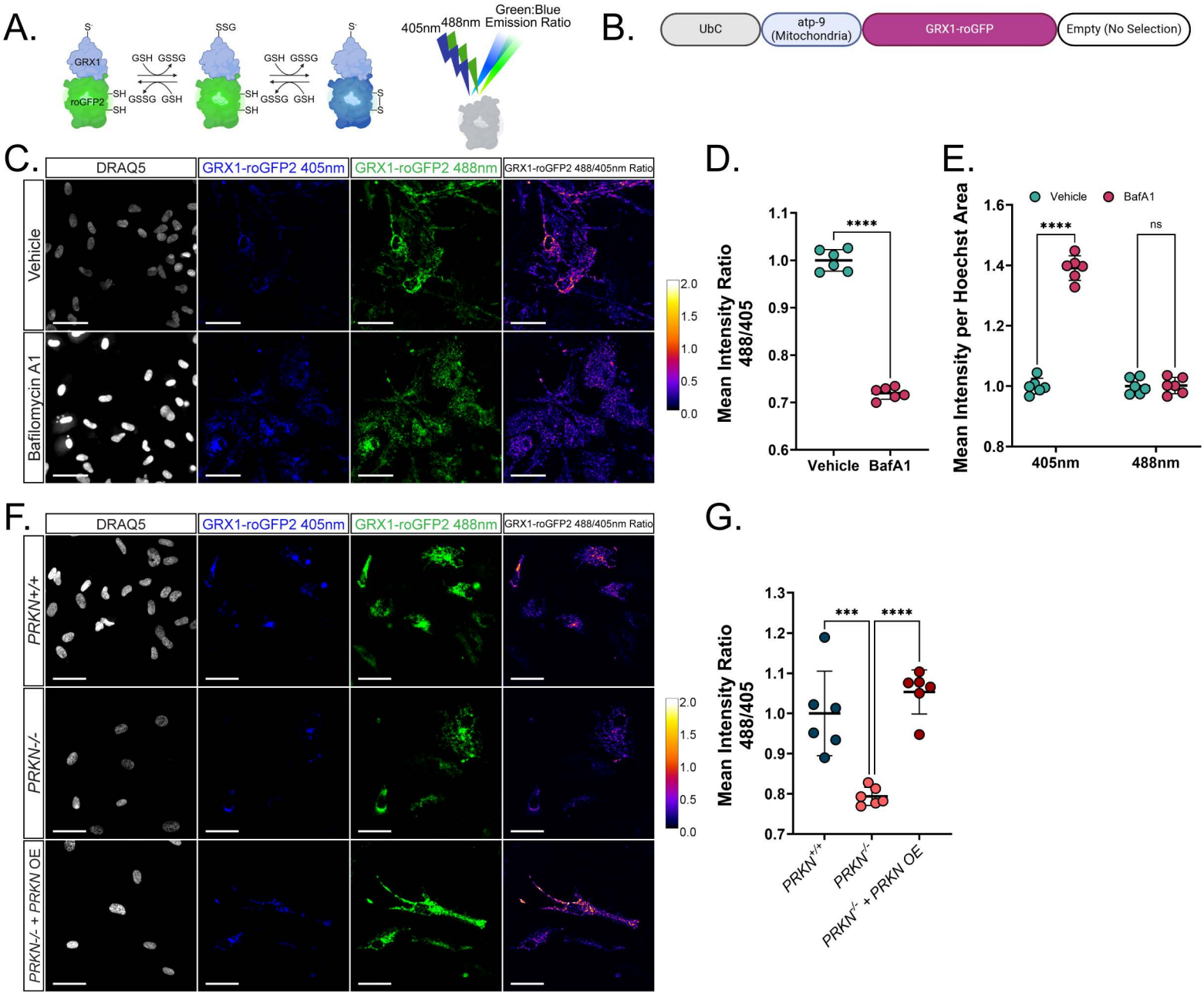
A.
GRX1
roGFP2
GSH GSSG
GSSG GSH
SSG
405nm
488nm
Green:Blue Emission Ratio
B.
UbC
atp-9 (Mitochondria)
GRX1-roGFP
Empty (No Selection)
C.
DRAQ5
GRX1-roGFP2 405nm
GRX1-roGFP2 488nm
GRX1-roGFP2 488/405nm Ratio
Vehicle
Bafilomycin A1
D.
Mean Intensity Ratio 488/405
****
Vehicle
BafA1
E.
Mean Intensity per Hoechst Area
Vehicle
BafA1
****
ns
405nm
488nm
F.
DRAQ5
GRX1-roGFP2 405nm
GRX1-roGFP2 488nm
GRX1-roGFP2 488/405nm Ratio
PRKN+/+
PRKN-/-
PRKN-/- + PRKN OE
G.
Mean Intensity Ratio 488/405
***
****
PRKN+/+
PRKN-/-
PRKN-/- + PRKN OE

Figure S1

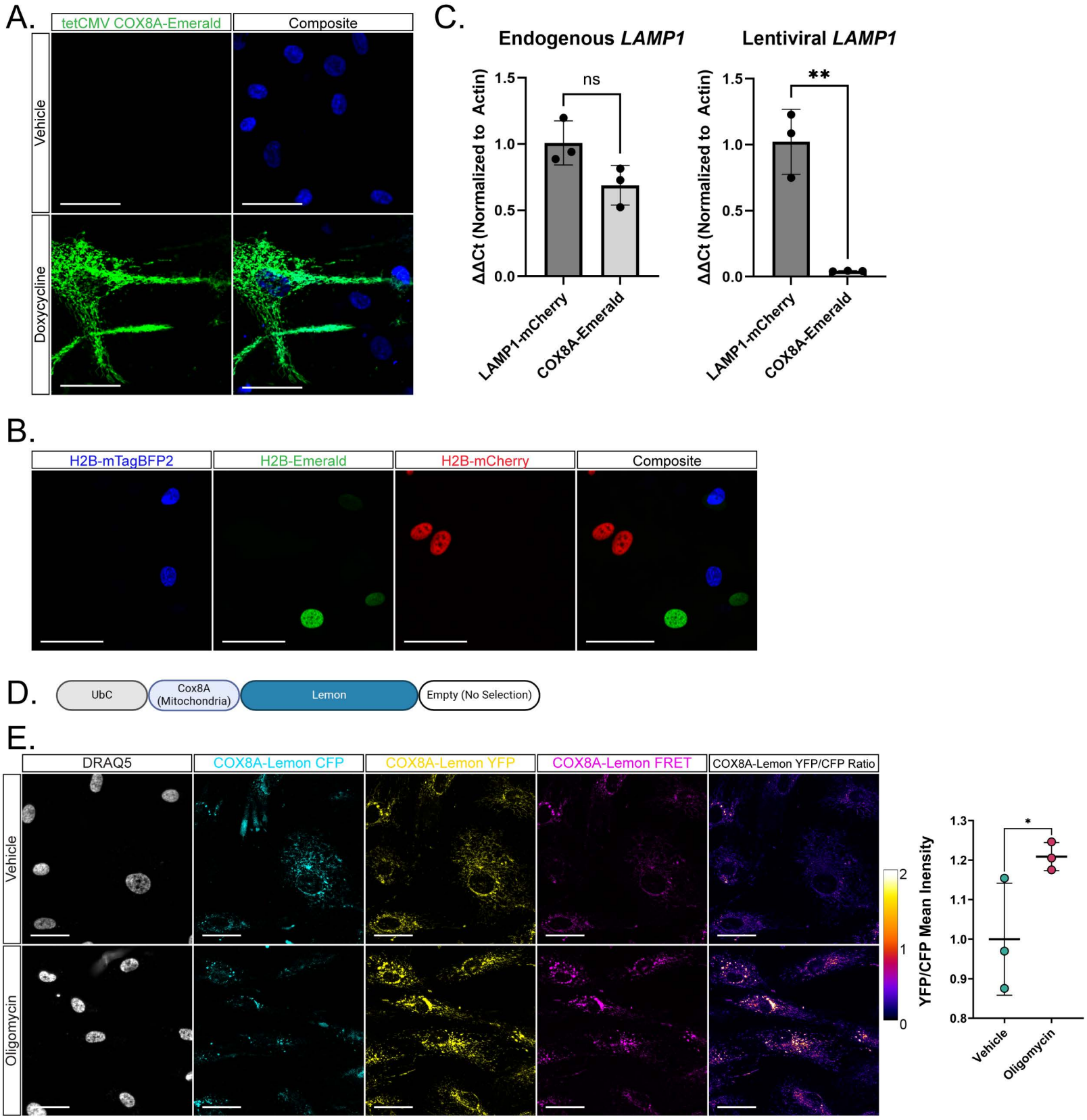
A.
tetCMV COX8A-Emerald
Composite
Vehicle
Doxycycline
C.
Endogenous LAMP1
Lentiviral LAMP1
ΔΔCt (Normalized to Actin)
ns
**
LAMP1-mCherry
COX8A-Emerald
B.
H2B-mTagBFP2
H2B-Emerald
H2B-mCherry
Composite
D.
UbC
Cox8A (Mitochondria)
Lemon
Empty (No Selection)
E.
DRAQ5
COX8A-Lemon CFP
COX8A-Lemon YFP
COX8A-Lemon FRET
COX8A-Lemon YFP/CFP Ratio
Vehicle
Oligomycin
YFP/CFP Mean Inensity
*

Figure S2

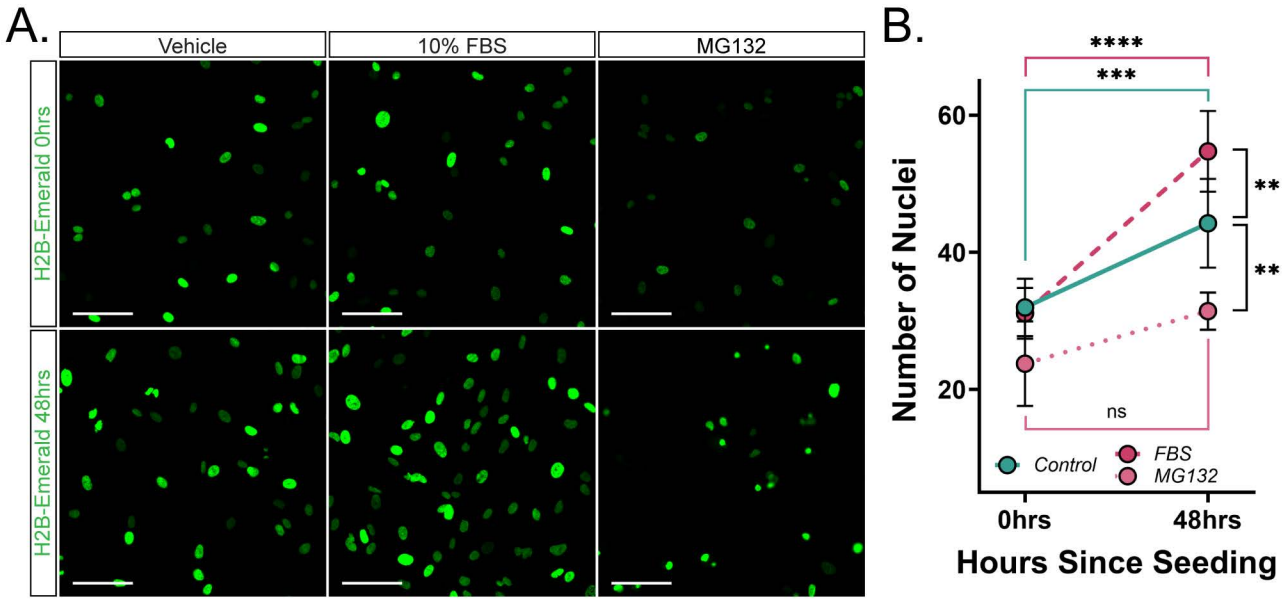
A.
Vehicle
10% FBS
MG132
H2B-Emerald 0hrs
H2B-Emerald 48hrs
B.
****
***
**
**
ns
60
40
20
Number of Nuclei
Control
FBS
MG132
0hrs
48hrs
Hours Since Seeding

Figure S3

A.

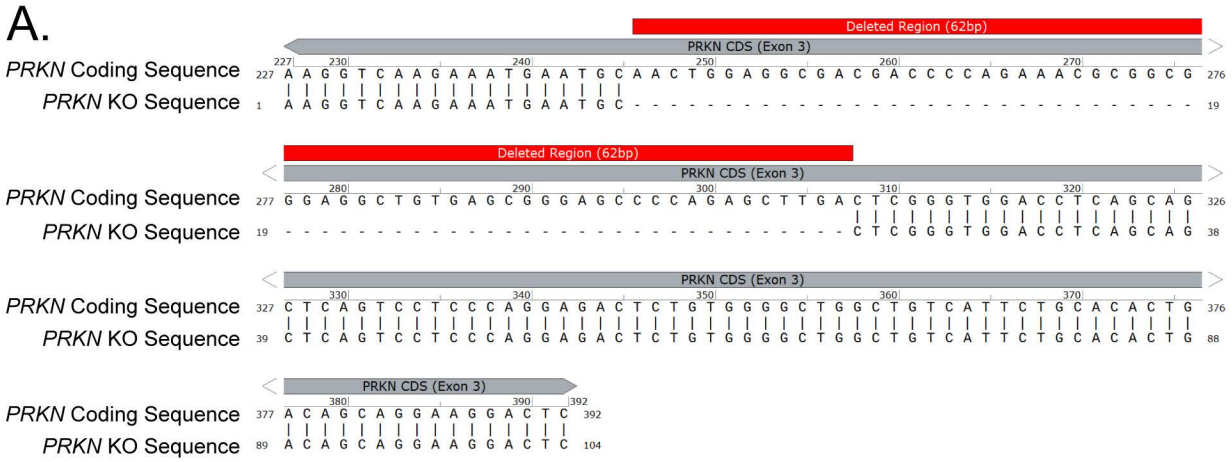
Deleted Region (62bp)
PRKN CDS (Exon 3)
PRKN Coding Sequence
PRKN KO Sequence
227 A A G G T C A A G A A A T G A A T G C A A C T G G A G G C G A C G A C C C C A G A A A C G C G G C G 276
1 A A G G T C A A G A A A T G A A T G C - 19
Deleted Region (62bp)
PRKN CDS (Exon 3)
PRKN Coding Sequence
PRKN KO Sequence
277 G G A G G C T G T G A G C G G G A G C C C C A G A G C T T G A C T C G G G T G G A C C T C A G C A G 326
19 - C T C G G G T G G A C C T C A G C A G 38
PRKN CDS (Exon 3)
PRKN Coding Sequence
PRKN KO Sequence
327 C T C A G T C C T C C C A G G A G A C T C T G T G G G G C T G G C T G T C A T T C T G C A C A C T G 376
39 C T C A G T C C T C C C A G G A G A C T C T G T G G G G C T G G C T G T C A T T C T G C A C A C T G 88
PRKN CDS (Exon 3)
PRKN Coding Sequence
PRKN KO Sequence
377 A C A G C A G G A A G G A C T C 392
89 A C A G C A G G A A G G A C T C 104

B.

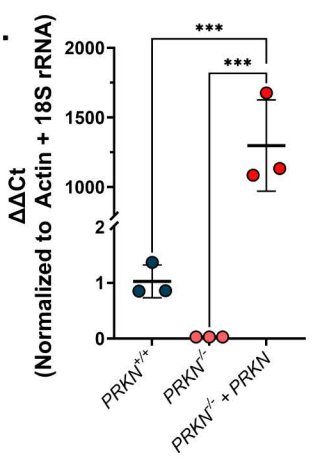
ΔΔCt
(Normalized to Actin + 18S rRNA)
2000
1500
1000
2
1
0
***
***
PRKN+/+
PRKN-/-
PRKN-/- + PRKN

Figure S4

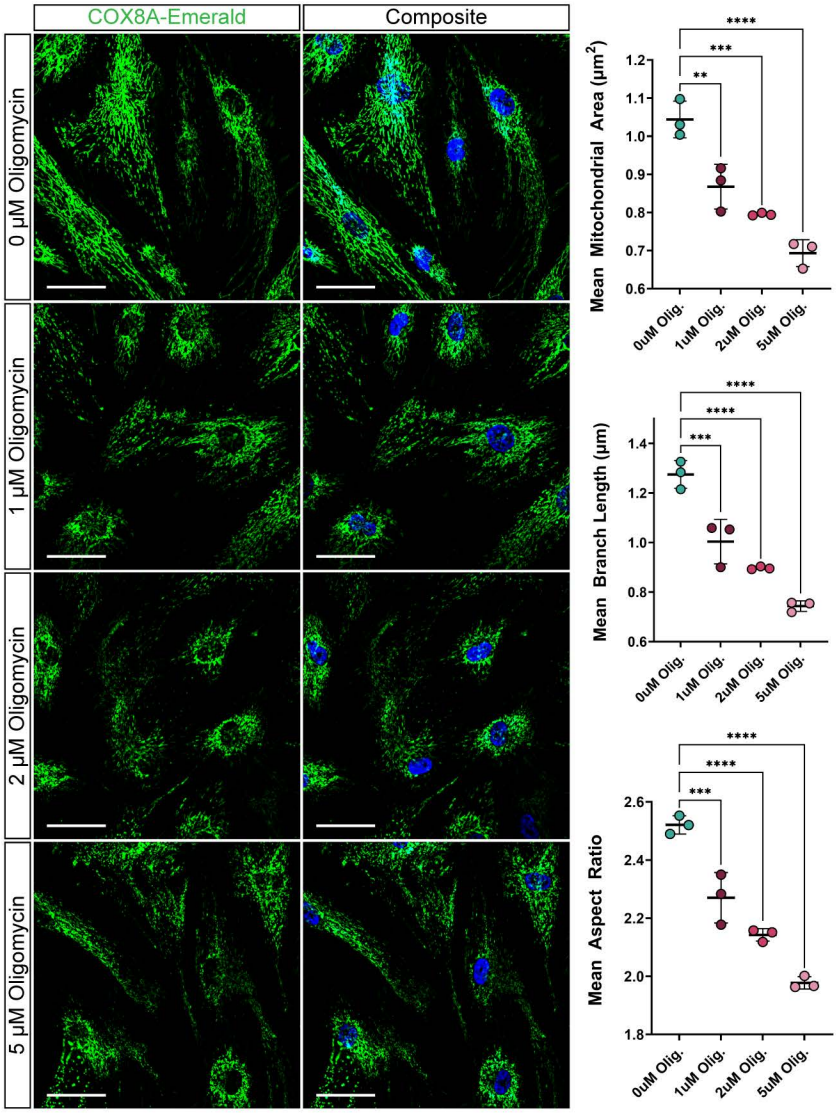
COX8A-Emerald
Composite
0 µM Oligomycin
1 µM Oligomycin
2 µM Oligomycin
5 µM Oligomycin
Mean Mitochondrial Area (µm²)
Mean Branch Length (µm)
Mean Aspect Ratio
0uM Olig.
1uM Olig.
2uM Olig.
5uM Olig.
**
***
****

Plasmid Name	AddGene ID	Localization	Fluorophore	Antibiotic Resistance	Relevant Figures
pFUW H2B-mTagBFP2-p2A-PuroR	239552	Nucleus	mTagBFP2	Puromycin	1, 2, S1
pFUW H2B-Emerald-p2A-PuroR	239553	Nucleus	Emerald	Puromycin	2, S1, S2
pFUW H2B-mCherry-p2A-PuroR	239554	Nucleus	mCherry	Puromycin	2, S1
pFUW LAMP1Sig-Emerald	239555	Lysosome	Emerald	NA	1, 3
pFUW LAMP1Sig-mCherry	239556	Lysosome	mCherry	NA	1
pFUW COX8ASig-Emerald	239557	Mitochondria	Emerald	NA	1, 4, S4
pFUW COX8ASig-mCherry	239558	Mitochondria	mCherry	NA	1
pFUW PuroR-P2A-COX8ASig-Timer	239559	Mitochondria	Timer	Puromycin	5
pFUW COX8ASig-Lemon	239560	Mitochondria	Lemon	NA	S1
pFUW mito-GRX1-roGFP2	239561	Mitochondria	roGFP2	NA	6
pFUW mTagBFP2	239562	NA	mTagBFP2	NA	NA
pFUW Emerald	239563	NA	Emerald	NA	NA
pFUW mCherry	239564	NA	mCherry	NA	NA
pFUW mTagBFP2-P2A-PuroR	239565	NA	mTagBFP2	Puromycin	NA
pFUW Emerald-P2A-PuroR	239566	NA	Emerald	Puromycin	3
pFUW mCherry-P2A-PuroR	239567	NA	mCherry	Puromycin	NA
pFUW mTagBFP2-P2A-NeoR	239568	NA	mTagBFP2	Neomycin	NA
pFUW Emerald-P2A-NeoR	239569	NA	Emerald	Neomycin	NA
pFUW mCherry-P2A-NeoR	239570	NA	mCherry	Neomycin	NA
pFUW PRKN-P2A-PuroR	239571	NA	NA	Puromycin	6, S3

Table S1: A list of all plasmids generated in this study. Details for all plasmids, including subcellular localization, fluorophore, antibiotic resistance, and in which figure each plasmid was used. More plasmids were generated as part of GEM-SCOPe than used in the final publication, and these are also included here and available on Addgene.